

ZONAL FLOWS AND LONG-LIVED AXISYMMETRIC PRESSURE BUMPS IN MAGNETOROTATIONAL TURBULENCE

A. JOHANSEN

Leiden Observatory, Leiden University, P.O. Box 9513, 2300 RA Leiden, The Netherlands

A. YOU DIN

Canadian Institute for Theoretical Astrophysics, University of Toronto, 60 St. George Street, Toronto, Ontario M5S 3H8, Canada

AND

H. KLAHR

Max-Planck-Institut für Astronomie, 69117 Heidelberg, Germany

Draft version November 6, 2018

ABSTRACT

We study the behavior of magnetorotational turbulence in shearing box simulations with a radial and azimuthal extent up to ten scale heights. Maxwell and Reynolds stresses are found to increase by more than a factor two when increasing the box size beyond two scale heights in the radial direction. Further increase of the box size has little or no effect on the statistical properties of the turbulence. An inverse cascade excites magnetic field structures at the largest scales of the box. The corresponding 10% variation in the Maxwell stress launches a zonal flow of alternating sub- and super-Keplerian velocity. This in turn generates a banded density structure in geostrophic balance between pressure and Coriolis forces. We present a simplified model for the appearance of zonal flows, in which stochastic forcing by the magnetic tension on short time-scales creates zonal flow structures with life-times of several tens of orbits. We experiment with various improved shearing box algorithms to reduce the numerical diffusivity introduced by the supersonic shear flow. While a standard finite difference advection scheme shows signs of a suppression of turbulent activity near the edges of the box, this problem is eliminated by a new method where the Keplerian shear advection is advanced in time by interpolation in Fourier space.

Subject headings: diffusion — hydrodynamics — instabilities — planetary systems: protoplanetary disks — solar system: formation — turbulence

1. INTRODUCTION

Turbulence forms a main pillar of modern accretion disk theory (see review by Balbus & Hawley 1998). The most promising turbulence candidate is the magnetorotational instability (MRI, Balbus & Hawley 1991), which renders Keplerian rotation profiles linearly unstable in the presence of a magnetic field of moderate strength. The non-linear evolution of the MRI is often modeled in a local, corotating box representing a small section of a Keplerian disk (e.g. Hawley et al. 1995; Brandenburg et al. 1995). This allows high resolution studies with periodic boundary conditions. However, most shearing box simulations have been limited to a narrow radial extent of approximately one scale height.

In this paper we explore shearing box simulations with a radial domain up to ten scale heights. Increasing the radial extent helps bridge the gap between smaller local simulations and global simulations of accretion disks (e.g. Armitage 1998; Arlt & Rüdiger 2001; Fromang & Nelson 2006; Lyra et al. 2008). Since rotating shear flows are prone to an inverse cascade of magnetic energy (Brandenburg & Subramanian 2005), large simulation domains are needed to fully capture the saturated state of the MRI.

We find that the statistical properties of magnetorotational turbulence converge relatively well as we increase the radial extent of the simulation box beyond a couple of scale heights. However, large shearing boxes do not behave simply like multiple copies of moderately sized boxes. Axisymmetric pressure bumps, in geostrophic balance with a sub-Keplerian/super-Keplerian zonal flow envelope, grow to fill the radial width of the box. A main purpose of this paper is to describe the excitation and dynamics of such zonal flows.

The emergence of zonal flows in protoplanetary disks can have a profound influence on the growth of terrestrial planets and giant planet cores. Planet formation begins as dust grains collide and grow to ever larger bodies (Safronov 1969; Dominik et al. 2007; Blum & Wurm 2008). Macroscopic solids drift rapidly through the disk, due to the head wind from the slightly sub-Keplerian gas (Weidenschilling 1977), imposing a severe time-scale constraint on the growth from approximately cm-sized pebbles to bodies several kilometers in size. A weak variation of the rotation profile caused by zonal flows may nevertheless suffice to locally stop the radial drift flow (Whipple 1972; Klahr & Lin 2001; Haghighipour & Boss 2003; Fromang & Nelson 2005; Kato et al. 2008). Such a convergence zone can quickly accumulate rocks and boulders, enhancing the local density enough to trigger gravitational instabilities which form planetesimals or dwarf planets in a very short time (Youdin & Shu 2002;

Electronic address: ajohan@strw.leidenuniv.nl
Electronic address: youd@cita.utoronto.ca
Electronic address: klahr@mpia.de

Johansen et al. 2006, 2007). The reduced radial drift due to persistent zonal flows may also facilitate dust growth by a longer time-scale coagulation-fragmentation process (Weidenschilling 1997; Dullemond & Dominik 2005; Brauer et al. 2008a,b; Johansen et al. 2008).

Turbulent density fluctuations exert significant gravitational torques on planetesimals and planetary embryos. This adds a stochastic element to the normally inward type-I planetary migration from gravitational interactions with the gas disk. Migration can be slowed, sped up, or even reversed, especially for lower mass planets (Nelson & Papaloizou 2004; Laughlin et al. 2004; Johnson et al. 2006; Oishi et al. 2007). Gravitational scattering can also pump planetesimal eccentricities to the level where collisions become destructive for small planetesimals with low surface gravity (Ida et al. 2008). The dominant *axisymmetric* component of the density fluctuations that we analyze in this paper exerts no gravitational torques. Thus non-axisymmetric modes – perhaps in global simulations – must be considered in a future publication for applications to planet migration and scattering.

Zonal flows arise in a diverse range of physical settings. The launching mechanism in the examples below differ, both from each other and from the problem at hand. A common feature is non-linear mode coupling and variation in turbulent transport coefficients over large length scales.

Giant planet atmospheres. The banded structure in Jupiter’s cloud layer is perhaps the most famous manifestation of zonal flows. Busse (1976) proposed that these flows arise from an inverse cascade of thermally driven convection in giant planet interiors. Simulations of convective turbulence in spherical shells (e.g., Sun et al. 1993; Heimpel & Aurnou 2007) reproduce the zonal flows in gas and ice giants both qualitatively and quantitatively.

Torsional oscillations. On top of the differential rotation profile of the Sun there is a zonal flow (with 3 m/s amplitude) that migrates from high to low latitudes during the solar cycle (Howard & Labonte 1980). The zonal flow is attributed to the toroidal component of the Lorentz force exerted by magnetic fields arising in the solar dynamo (Schüssler 1981; Yoshimura 1981).

Laboratory plasmas. Laboratory plasmas often exhibit strong zonal flows. These self-organized structures arise from a non-local inverse cascade mediated by drift waves. The excellent review by Diamond et al. (2005) points out the intimate mathematical equivalence between Rossby wave dynamics in planetary atmospheres and drift wave dynamics in plasmas.

In magnetorotational accretion disk turbulence we find that the zonal flow is excited by a large scale variation in the Maxwell stress. The differential momentum transport by the associated magnetic tension launches the sub-Keplerian/super-Keplerian zonal flows, which in turn are slightly compressive and form pressure bumps with lifetimes approximately equal to the turbulent mixing time-scale. The variation in the Maxwell stress is a consequence of an inverse cascade of magnetic energy to the largest scales of the box.

Practical numerical issues arise in simulations of large shearing boxes, since the supersonic orbital shear introduces significant numerical diffusivity. In simulations

of magnetorotational turbulence, Johnson et al. (2008) found a spurious density depression in the radial center of the grid. Here the velocity of the shear flow vanishes, minimizing numerical dissipation, and the local increase in turbulent stresses leads to a mass transport away from the box center. We also find indications of this unphysical behavior in our biggest simulations, if we use the standard shearing box solver of the Pencil Code. However we can essentially eliminate this undesired effect with two independent techniques described in the appendices: (1) separately solving the known advection by orbital shear with high order interpolation or (2) displacing the entire grid systematically in the radial direction so that preferred locations in the box vary too rapidly to generate artificial structures. This gives us confidence that the zonal flows we see are not a numerical artifact.

The structure of the paper is as follows. In §2 we describe the shearing box coordinate frame, dissipation operators and simulation parameters. The properties of turbulence in large shearing boxes are presented in §3. The following section, §4, is dedicated to describing the large scale zonal flows that are ubiquitous to the simulations. In §5 we present a simplified model for the stochastic excitation of zonal flows. The radial variation in Maxwell stress and the inverse cascade of magnetic energy is discussed in detail in §6. In §7 we validate our results by presenting convergence tests, variations of the main simulations using different shearing box algorithms, and the dependence of the zonal flows on the order and magnitude of the explicit dissipation. In §8 we summarize our results briefly and discuss caveats and implications. The appendices contain a test of the shearing box solver (Appendix A), a description of a newly developed technique to interpolate Keplerian advection in wavenumber space (Appendix B), and additional techniques to reduce space-dependent numerical diffusivity (Appendix C).

2. MODEL SETUP

We simulate a local, corotating patch of a Keplerian disk in the shearing box approximation. The axes are oriented such that x points outwards along the cylindrical radius, y points along the main rotation direction, and z points vertically out of the disk parallel to the Keplerian rotation vector Ω . The criterion for the validity of the shearing box approximation is strictly that the box size L should be much smaller than the orbital radius r , so that curvature terms may be ignored. In practice this implies that the box size measured in scale heights, L/H , must be much smaller than the inverse aspect ratio of the disk, $(L/H) \ll 1/(H/r)$. For typical values $(H/r) = 0.01 \dots 0.1$ we get $(L/H) \ll 10 \dots 100$. We shall consider boxes with a radial extent of up to ten times the scale height, which is still fairly well represented in the shearing box approximation. We have chosen the shearing box approximation over global disk simulations because of the absence of boundaries and because it makes it possible to study convergence in resolution and box size from a relatively well understood coordinate frame.

The ideal MHD equation of motion, for the velocity field \mathbf{u} relative to the linearized Keplerian shear, is

$$\frac{\partial \mathbf{u}}{\partial t} + (\mathbf{u} \cdot \nabla) \mathbf{u} + u_y^{(0)} \frac{\partial \mathbf{u}}{\partial y} = 2\Omega u_y \mathbf{e}_x - \frac{1}{2} \Omega u_x \mathbf{e}_y - \Omega^2 z \mathbf{e}_z$$

$$+\frac{1}{\rho}\mathbf{J}\times\mathbf{B}-\frac{1}{\rho}\nabla P+\mathbf{f}_\nu(\mathbf{u},\rho). \quad (1)$$

The left hand side of the equation contains the advection by the perturbed velocity \mathbf{u} and by the Keplerian shear flow $u_y^{(0)}\mathbf{e}_y$, where $u_y^{(0)} = -(3/2)\Omega x$. The right hand side contains the usual terms for Coriolis force, vertical component of the gravity of the central object, Lorentz force, pressure gradient force and an explicit viscosity term \mathbf{f}_ν constructed to dissipate the kinetic energy released by Reynolds and Maxwell stresses (see §2.1 for details). The magnetic field is calculated from the magnetic vector potential through $\mathbf{B} = \nabla \times \mathbf{A}$, and the current density is calculated through Ampere's law $\mathbf{J} = \mu_0^{-1}\nabla \times (\nabla \times \mathbf{A})$.

The magnetic vector potential \mathbf{A} is evolved through the uncurled induction equation

$$\frac{\partial \mathbf{A}}{\partial t} + u_y^{(0)} \frac{\partial \mathbf{A}}{\partial y} = \mathbf{u} \times \mathbf{B} + \frac{3}{2}\Omega A_y \mathbf{e}_x + \mathbf{f}_\eta(\mathbf{A}). \quad (2)$$

The terms on the right hand side are the electromotive force and an explicit magnetic stretching term representing the creation of A_x from A_y (conversely creation of B_y from B_x) by the Keplerian shear. Explicit resistivity is taken into account through the term \mathbf{f}_η (see §2.1). For simulations with a weak imposed vertical field, we add a constant field $\langle B_z \rangle \mathbf{e}_z$ to the magnetic field \mathbf{B} appearing in the electromotive force in equation (2) and in the Lorentz force in equation (1). In the analysis of our results we will seek to understand the evolution of the magnetic field via the action of individual terms from the induction equation for \mathbf{B} , so we give it here for reference,

$$\frac{\partial \mathbf{B}}{\partial t} + (\mathbf{u} \cdot \nabla) \mathbf{B} + u_y^{(0)} \frac{\partial \mathbf{B}}{\partial y} = (\mathbf{B} \cdot \nabla) \mathbf{u} - \frac{3}{2}\Omega B_x \mathbf{e}_y - \mathbf{B} \nabla \cdot \mathbf{u}. \quad (3)$$

The advection terms appear in their usual form on the left hand side. The terms on the right hand side of equation (3) are the internal stretching term, the Keplerian stretching term, and the compression term.

Finally the mass density ρ is evolved through the continuity equation

$$\frac{\partial \rho}{\partial t} + \mathbf{u} \cdot \nabla \rho + u_y^{(0)} \frac{\partial \rho}{\partial y} = -\rho \nabla \cdot \mathbf{u} + f_D(\rho). \quad (4)$$

The last term on the right hand side is an explicit mass diffusion term (presented in §2.1). We use an isothermal equation of state, $P = c_s^2 \rho$, to connect the pressure P and the density ρ . The soundspeed c_s is assumed to be constant.

As a numerical solver we use the 6th order symmetric finite difference code Pencil Code¹. In Appendix A we test the standard shearing box algorithm of the Pencil Code against a time-dependent analytical solution (Balbus & Hawley 2006) for a shearing wave and find excellent agreement. We also compare the evolution of a low amplitude, magnetized shear wave to a numerical integration of the linearized evolution equations. However, while the tests in Appendix A give confidence that the Pencil Code solves the shearing box equations correctly,

they are not sufficient to fully validate our non-linear simulations. For this we will present the main results using several independent shearing box algorithms. Normally we use the same finite difference advection scheme for the Keplerian shear advection as for any other advection term, but we have also implemented the Keplerian advection as an interpolated shift of the dynamical variables (similar to Masset 2000; Gammie 2001; Johnson et al. 2008). This has the advantage that the space-dependence of the numerical diffusivity is removed and that the time-step constraint connected with the Keplerian shear flow is eased. Our new Shear Advection by Fourier Interpolation (SAFI) scheme, described in detail in Appendix B, differs from other shear advection schemes in that interpolation is done in Fourier space, yielding essentially perfect interpolation of sufficiently smooth flows when shifting a mode by any arbitrary fraction of a grid cell. Two additional algorithms for reducing the space-dependence of the numerical dissipation are presented in Appendix C.

2.1. Dissipation

The symmetric finite difference scheme of the Pencil Code has very little intrinsic amplitude error (i.e. numerical diffusion) in the advection terms (Brandenburg 2003). Therefore we must add explicit dissipation terms to the evolution equations in order to get rid of the kinetic and magnetic energy, released from the gravitational potential by Reynolds and Maxwell stresses, on the smallest scales of the grid.

2.1.1. Viscosity

The viscosity term \mathbf{f}_ν appears in full generality as

$$\begin{aligned} \mathbf{f}_\nu = & \nu_1 \left[\nabla^2 \mathbf{u} + \frac{1}{3} \nabla \nabla \cdot \mathbf{u} + 2(\mathbf{S}^{(1)} \cdot \nabla \ln \rho) \right] \\ & + \nu_3 \left[\nabla^6 \mathbf{u} + (\mathbf{S}^{(3)} \cdot \nabla \ln \rho) \right] \\ & + \nu_{\text{sh}} \left[\nabla \nabla \cdot \mathbf{u} + (\nabla \cdot \mathbf{u})(\nabla \ln \rho) \right] + (\nabla \nu_{\text{sh}}) \nabla \cdot \mathbf{u}. \end{aligned} \quad (5)$$

The viscosity includes regular Navier-Stokes viscosity with constant coefficient ν_1 , hyperviscosity with constant coefficient ν_3 and shock viscosity with a variable coefficient ν_{sh} . In general we include only a subset of the three types of viscosity, representing both direct numerical simulations (DNS) and combined hyperviscosity/shock viscosity solution of the equation of motion. In the following paragraphs we discuss the three types of viscosity in more detail.

Navier-Stokes viscosity (ν_1): Since the density is not nearly constant in the stratified models, we must add a density dependent term $2(\mathbf{S}^{(1)} \cdot \nabla \ln \rho)$ to equation (5) in order to conserve momentum. Here the traceless rate-of-strain tensor $\mathbf{S}^{(1)}$ is

$$S_{ij}^{(1)} = \frac{1}{2} \left(\frac{\partial u_i}{\partial x_j} + \frac{\partial u_j}{\partial x_i} - \frac{2}{3} \delta_{ij} \nabla \cdot \mathbf{u} \right). \quad (6)$$

Hyperviscosity (ν_3): A simplified third order rate-of-strain tensor $\mathbf{S}^{(3)}$ is here defined as

$$S_{ij}^{(3)} = \frac{\partial^5 u_i}{\partial x_j^5}. \quad (7)$$

The high order Laplacian ∇^6 in equation (5) is expanded as $\nabla^6 = \partial^6/\partial x^6 + \partial^6/\partial y^6 + \partial^6/\partial z^6$. This form of the

¹ The code is accessible for download at <http://www.nordita.org/software/pencil-code/>; see Brandenburg (2003) for details on the numerical algorithm of the Pencil Code.

TABLE 1
RUN PARAMETERS

Run	$L_x \times L_y \times L_z$	$N_x \times N_y \times N_z$	ν_i	η_i	Order	Strat.	$\langle B_z \rangle$	Shear	Δt
S	$1.32 \times 1.32 \times 5.28$	$32 \times 32 \times 128$	6.0×10^{-10}	6.0×10^{-10}	3	Yes	0.0	FDA	100
M	$2.64 \times 2.64 \times 5.28$	$64 \times 64 \times 128$	6.0×10^{-10}	6.0×10^{-10}	3	Yes	0.0	FDA	100
L	$5.28 \times 5.28 \times 5.28$	$128 \times 128 \times 128$	6.0×10^{-10}	6.0×10^{-10}	3	Yes	0.0	SAFI	100
H	$10.56 \times 10.56 \times 5.28$	$256 \times 256 \times 128$	6.0×10^{-10}	6.0×10^{-10}	3	Yes	0.0	SAFI	100
M_r2	$2.64 \times 2.64 \times 5.28$	$128 \times 128 \times 256$	2.0×10^{-11}	2.0×10^{-11}	3	Yes	0.0	FDA	100
L_nogz	$5.28 \times 5.28 \times 5.28$	$128 \times 128 \times 128$	6.0×10^{-10}	6.0×10^{-10}	3	No	0.0	SAFI	100
M_Bz_r0.5	$2.64 \times 2.64 \times 5.28$	$32 \times 32 \times 64$	2.0×10^{-8}	2.0×10^{-8}	3	Yes	0.01	FDA	100
M_Bz	$2.64 \times 2.64 \times 5.28$	$64 \times 64 \times 128$	6.0×10^{-10}	6.0×10^{-10}	3	Yes	0.01	FDA	100
M_Bz_r2	$2.64 \times 2.64 \times 5.28$	$128 \times 128 \times 256$	2.0×10^{-11}	2.0×10^{-11}	3	Yes	0.01	FDA	50
MS	$2.64 \times 2.64 \times 1.32$	$64 \times 64 \times 32$	6.0×10^{-10}	6.0×10^{-10}	3	No	0.0	SRD	100
MS_r2	$2.64 \times 2.64 \times 1.32$	$128 \times 128 \times 64$	2.0×10^{-11}	2.0×10^{-11}	3	No	0.0	FDA	100
MS_r2_fix	$2.64 \times 2.64 \times 1.32$	$128 \times 128 \times 64$	6.0×10^{-10}	6.0×10^{-10}	3	No	0.0	SRD	100
SS_r4_nu1	$1.32 \times 1.32 \times 1.32$	$128 \times 128 \times 128$	3.0×10^{-4}	8.0×10^{-5}	1	No	0.0	FDA	40
SS_r8_nu1	$1.32 \times 1.32 \times 1.32$	$256 \times 256 \times 256$	3.0×10^{-4}	8.0×10^{-5}	1	No	0.0	FDA	25
MS_r4_nu1	$2.64 \times 2.64 \times 1.32$	$256 \times 256 \times 128$	3.0×10^{-4}	8.0×10^{-5}	1	No	0.0	FDA	50

NOTE. — Col. (1): Name of run. Col. (2): Box size in units of scale heights. Col. (3): Grid resolution. Col. (4): Viscosity coefficient. Col. (5): Resistivity coefficient. Col. (6): Dissipation order. Col. (7): Stratification. Col. (8): Mean imposed vertical field. Col. (9): Shear advection scheme. Col. (10): Total run time in orbits ($T_{\text{orb}} = 2\pi\Omega^{-1}$).

hyperviscosity conserves momentum (Johansen & Klahr 2005), but the energy dissipation is not guaranteed to be positive by mathematical construction, nor is the rate-of-strain tensor symmetric. We therefore compared all our results with the evolution obtained by using a strict hyperviscosity operator (following Haugen & Brandenburg 2004) and found no qualitative differences, so we opted to use the simplified hyperviscosity because it is much simpler and quicker than the full version.

Shock viscosity (ν_{sh}): The stratified runs produce shocks high up in the atmosphere of the disk. In order to dissipate sufficient energy in the shocks, without rendering the whole simulation domain strongly viscous, we have added an additional shock viscosity term. The shock viscosity coefficient is obtained in a von Neumann-Richtmyer fashion by taking the negative part of the divergence of \mathbf{u} , then taking the maximum over three grid cells in each direction, and finally averaging over three grid cells, to obtain

$$\nu_{\text{sh}} = c_{\text{sh}} \langle \max[-\nabla \cdot \mathbf{u}]_+ \rangle (\delta x)^2. \quad (8)$$

We set the shock viscosity coefficient to $c_{\text{sh}} = 1.0$ in the stratified runs to dissipate energy in shocks forming above two scale heights from the mid-plane of the disk. The shock viscosity ν_{sh} decreases rapidly with increasing resolution, so convergence tests also probe the effect of decreasing the shock viscosity term.

2.1.2. Resistivity

For the resistivity term \mathbf{f}_η we consider either normal resistivity or hyperresistivity,

$$\mathbf{f}_\eta = \eta_1 \nabla^2 \mathbf{A} + \eta_3 \nabla^6 \mathbf{A}. \quad (9)$$

As for the hyperviscosity we use a simplified version for ∇^6 , but checked that the strict high order Laplacian $\nabla^2 \nabla^2 \nabla^2$ gives qualitatively and quantitatively similar results.

2.1.3. Diffusion

Mass diffusion consists of hyperdiffusion and shock diffusion

$$f_D = D_3 \nabla^6 \rho + D_{\text{sh}} \nabla^2 \rho + \nabla D_{\text{sh}} \cdot \nabla \rho, \quad (10)$$

where $D_{\text{sh}} = \nu_{\text{sh}}$ is defined in equation (8). Mass diffusion turned out to be necessary in order to damp out spurious small-scale modes that are left behind due to the dispersion error in the finite differencing of the advection term in the continuity equation. We also add a bit of extra mass diffusion in the stratified simulations to stabilize the shocks forming above two scale heights from the mid-plane of the disk (setting the shock diffusion coefficient $D_{\text{sh}} = 1.0$ in Eq. [10]).

2.2. Boundary Conditions

We use the usual shearing box boundary conditions in the radial and azimuthal directions (shear-periodic/periodic). At the upper and lower boundaries we apply periodic boundary conditions, conserving the average flux of all components of the magnetic field. This turned out to be numerically less challenging, and we checked that perfect conductor boundary conditions ($\partial B_x / \partial z = \partial B_y / \partial z = B_z = 0$) and vertical field boundary conditions ($B_x = B_y = \partial B_z / \partial z = 0$) for the magnetic field give results that are qualitatively and quantitatively similar to what we see with periodic boundary conditions.

2.3. Simulation Parameters

We run simulations for various box sizes, resolutions, dissipation parameters, and imposed magnetic field strengths. The simulation parameters are given in Table 1. The main simulations are the stratified S, M, L, and H runs. These all share a vertical extent of $L_z = 5.28H$, but the radial/azimuthal extent of the box is varied in steps of two, from $L_x = L_y = 1.32$ in the smallest box² (S) to $L_x = L_y = 10.56$ in the largest box

² The choice of $L = 1.32$ as the basic box size unit is based on the fact that $L_x = 1.32$ approximately marks the transition from subsonic to supersonic Keplerian shear flow.

TABLE 2
 TURBULENCE PROPERTIES

Run	$\langle \frac{1}{2} \rho u_x^2 \rangle$	$\langle \frac{1}{2} \rho u_y^2 \rangle$	$\langle \frac{1}{2} \rho u_z^2 \rangle$	$\langle \frac{1}{2} B_x^2 \rangle$	$\langle \frac{1}{2} B_y^2 \rangle$	$\langle \frac{1}{2} B_z^2 \rangle$	$\langle \rho u_x u_y \rangle$	$\langle -B_x B_y \rangle$	α
S	1.9×10^{-3}	1.7×10^{-3}	1.5×10^{-3}	1.2×10^{-3}	9.1×10^{-3}	5.3×10^{-4}	1.1×10^{-3}	4.3×10^{-3}	0.0036
M	3.9×10^{-3}	5.1×10^{-3}	2.7×10^{-3}	4.2×10^{-3}	3.6×10^{-2}	2.1×10^{-3}	2.6×10^{-3}	1.2×10^{-2}	0.0097
L	4.0×10^{-3}	4.5×10^{-3}	2.4×10^{-3}	3.7×10^{-3}	2.6×10^{-2}	2.0×10^{-3}	2.5×10^{-3}	1.1×10^{-2}	0.0089
H	4.5×10^{-3}	4.2×10^{-3}	2.4×10^{-3}	3.5×10^{-3}	2.3×10^{-2}	1.8×10^{-3}	2.6×10^{-3}	1.0×10^{-2}	0.0085
M_r2	2.1×10^{-3}	2.8×10^{-3}	1.4×10^{-3}	2.3×10^{-3}	1.5×10^{-2}	1.2×10^{-3}	1.3×10^{-3}	6.5×10^{-3}	0.0052
L_nogz	3.2×10^{-3}	2.5×10^{-3}	1.4×10^{-3}	1.9×10^{-3}	1.3×10^{-2}	7.1×10^{-4}	1.8×10^{-3}	6.9×10^{-3}	0.0058
M_Bz_r0.5	5.8×10^{-3}	7.6×10^{-3}	4.0×10^{-3}	6.1×10^{-3}	6.6×10^{-2}	3.3×10^{-3}	3.8×10^{-3}	1.8×10^{-2}	0.0148
M_Bz	5.9×10^{-3}	1.0×10^{-2}	4.7×10^{-3}	1.1×10^{-2}	7.2×10^{-2}	6.8×10^{-3}	4.1×10^{-3}	2.5×10^{-2}	0.0196
M_Bz_r2	5.7×10^{-3}	1.2×10^{-2}	5.0×10^{-3}	1.2×10^{-2}	6.7×10^{-2}	7.8×10^{-3}	4.0×10^{-3}	2.7×10^{-2}	0.0207
MS	2.9×10^{-3}	2.0×10^{-3}	1.2×10^{-3}	1.4×10^{-3}	1.0×10^{-2}	4.6×10^{-4}	1.5×10^{-3}	5.2×10^{-3}	0.0045
MS_r2	1.7×10^{-3}	1.2×10^{-3}	7.2×10^{-4}	9.1×10^{-4}	5.7×10^{-3}	3.4×10^{-4}	8.4×10^{-4}	3.2×10^{-3}	0.0027
MS_r2_fix	3.4×10^{-3}	2.1×10^{-3}	1.7×10^{-3}	1.4×10^{-3}	9.1×10^{-3}	6.2×10^{-4}	1.5×10^{-3}	5.3×10^{-3}	0.0046
SS_r4_nu1	6.5×10^{-4}	6.1×10^{-4}	4.2×10^{-4}	5.1×10^{-4}	6.3×10^{-3}	1.8×10^{-4}	4.0×10^{-4}	2.8×10^{-3}	0.0021
SS_r8_nu1	1.0×10^{-3}	9.9×10^{-4}	7.1×10^{-4}	8.7×10^{-4}	8.9×10^{-3}	3.3×10^{-4}	6.6×10^{-4}	4.2×10^{-3}	0.0033
MS_r4_nu1	1.9×10^{-3}	1.8×10^{-3}	8.7×10^{-4}	1.5×10^{-3}	1.4×10^{-2}	5.1×10^{-4}	1.2×10^{-3}	6.8×10^{-3}	0.0053

 NOTE. — Col. (1): Name of run. Col. (2)-(4): Kinetic energy. Col. (5)-(7): Magnetic energy. Col. (8): Reynolds stress. Col. (9): Maxwell stress. Col. (10): α -value. Energies and stresses have been normalized with the mean thermal pressure in the box, $\langle P \rangle = c_s^2 \langle \rho \rangle$.

(H). For the M run we perform a convergence test by doubling the resolution (M_r2), and we also present an unstratified version of run L (L_nogz), ignoring the $-\Omega^2 z$ term in equation (1). The two largest box sizes (runs L, L_nogz and H) are evolved using the interpolated Keplerian shear scheme SAFI, described in Appendix B. This is done in order to relax the relatively tight time-step constraint of the Keplerian advection in these large boxes and at the same time remove the numerical diffusivity associated with the Keplerian advection.

The next group of simulations in Table 1, runs M_Bz_r0.5, M_Bz, M_Bz_r2, have a weak vertical magnetic field imposed on the gas, to keep the turbulent activity relatively constant when increasing the resolution. This makes it possible to better tell what effect resolution has on the zonal flows. In the unstratified runs MS, MS_r2 and MS_r2_fix, on the other hand, turbulent activity is maintained when keeping the hyperdissipation parameters constant as the resolution is increased.

The final set of simulations, runs SS_r4_nu1, SS_r8_nu1, MS_r4_nu1, apply more natural second derivative viscosity and resistivity operators to dissipate energy. A relatively high base resolution is needed here, as otherwise there are not enough small scales for the second order operators to dissipate kinetic and magnetic energy on. Strong zonal flows appear also with second derivative dissipation terms, and we see relatively good convergence in the zonal flow structure up to our highest resolution of around 200 grid points per scale height (eight times higher than the S – H runs).

2.4. Units and Initial Conditions

Throughout the paper we will state length in units of the scale height H , velocity in units of the isothermal sound speed c_s , time in units of the inverse Keplerian frequency Ω^{-1} or the orbital period $T_{\text{orb}} = 2\pi\Omega^{-1}$, density in units of the mid-plane density ρ_0 and magnetic field in units of $c_s(\mu_0\rho_0)^{1/2}$, related to the square root of the thermal pressure. Energies and stresses are always normalized by the mean thermal pressure in the box, $\langle P \rangle = c_s^2 \langle \rho \rangle$.

In the stratified runs we set the initial condition for

the density through an isothermal hydrostatic equilibrium with scale height $H = c_s/\Omega$, whereas the density is simply initialized to be constant in the non-stratified runs. The toroidal component of the magnetic vector potential is set as a moderate scale wave $A_y = A_0 \cos(k_x x) \cos(k_y y) \cos(k_z z)$ of amplitude $A_0 = 0.04$ and wave number $k_x = k_y = k_z = 4.76H^{-1}$, yielding an initial plasma β of around 50. We perturb the gas velocity components with random fluctuations of amplitude $\delta u \sim 10^{-3}c_s$.

3. TURBULENCE PROPERTIES IN LARGE SHEARING BOXES

The measured properties of the turbulent velocity and magnetic fields are written in Table 2. All quantities have been normalized by the average pressure in the box, $\langle P \rangle = c_s^2 \langle \rho \rangle$, for better comparison between stratified and non-stratified runs. The last column of Table 2 indicates the α -value of the flow (Shakura & Sunyaev 1973), defined through the Reynolds and Maxwell stress as

$$\alpha = \frac{2}{3} \frac{\langle (\rho u_x u_y - B_x B_y) \rangle}{\langle P \rangle}. \quad (11)$$

The time evolution of kinetic energy, magnetic energy and turbulent stresses for the standard runs S, M and L is plotted in Fig. 1. During the first orbit there is a sharp increase in both kinetic and magnetic energies, followed by a rapid drop. After the drop the energies climb slowly towards their saturation values, which are reached after around 20 orbits. In the saturated state there is more than a doubling of the energies and stresses when increasing the box size from $L_x = L_y = 1.32$ (S) to $L_x = L_y = 2.64$ (M), but little difference between run M and the twice as large run L. The vertical extent of the box is fixed at $L_z = 5.28$ in all the simulations. The kinetic energy is distributed relatively isotropically in the three components in the small box. But a distinct split into a high radial/azimuthal contribution and a low vertical contribution is seen when going to larger computational domains. This split indicates a transition to scales dominated by the Coriolis force, as geostrophic modes excited by the turbulence involve only in-plane

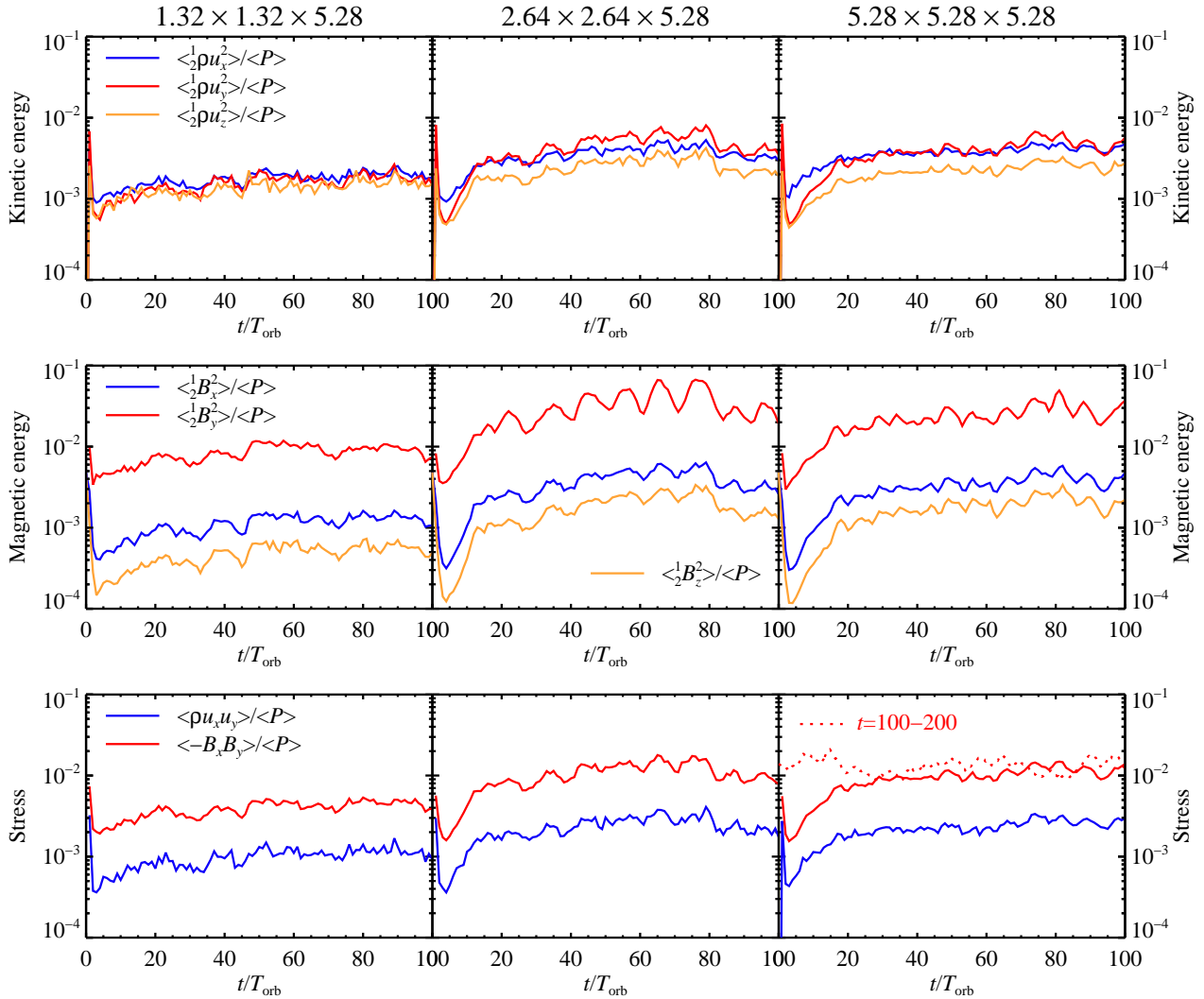


FIG. 1.— Kinetic energy (top row), magnetic energy (middle row) and turbulent stresses (bottom row) as a function of time measured in orbits, shown for three different box sizes along the columns (standard runs S, M and L). All quantities have been normalized by the mean thermal pressure in the box. Energies and stresses increase by more than a factor two when doubling the box dimensions from $L_x = L_y = 1.32H$ to $L_x = L_y = 2.64H$, but another doubling makes no significant difference for the statistical properties of the turbulence. The dotted line in the lower, right panel indicates the further evolution of the Maxwell stress from $t = 100T_{\text{orb}}$ to $t = 200T_{\text{orb}}$, showing that the turbulent stresses in run L remain fairly constant after $t = 30T_{\text{orb}}$.

gas motion.

The magnetic field is dominated by the azimuthal component for all domain sizes, as expected since Keplerian shear stretches radial field and creates azimuthal field of order $|\hat{B}_y| \sim (t_{\text{coh}}/t_{\text{shear}})|\hat{B}_x|$, where t_{coh} is the coherence time of the radial field and $t_{\text{shear}} = (2/3)\Omega^{-1}$ is the shear time-scale. The ratio $\text{rms}(B_y)/\text{rms}(B_x) \approx 2.5\text{--}3.0$ for runs S–H gives a (scale averaged) coherence time-scale of $t_{\text{coh}} \approx 2\Omega^{-1}$. Based on the long correlation time of large scale density and velocity structures (§4), one might expect an even greater dominance of B_y , especially in the larger boxes. However, the large scale zonal flow is built up from small, uncorrelated kicks by the Lorentz force, and a relatively short correlation time of the magnetic field fits well into this random walk picture.

Maxwell and Reynolds stresses increase from $\langle \rho u_x u_y \rangle \approx 0.001$ and $\langle -B_x B_y \rangle \approx 0.004$ in the

smallest box to $\langle \rho u_x u_y \rangle \approx 0.0025$ and $\langle -B_x B_y \rangle \approx 0.01$ in the largest box, yielding an increase in α -value from $\alpha \approx 0.004$ to $\alpha \approx 0.009$. This increase is of interest because global simulations of the MRI tend to yield higher α -values than traditional narrow shearing boxes (Hawley et al. 1995; Brandenburg et al. 1995; Arlt & Rüdiger 2001; Fromang & Nelson 2006). Our simulations suggest a transition towards the global value with increasing size of the shearing box. An additional explanation for the measured high stresses in global simulations may be the relatively low resolution per scale height possible in these simulations. The saturated state of non-stratified zero net vertical flux magnetorotational turbulence has been shown to decline with increasing resolution (Fromang & Papaloizou 2007), due to the change in numerical dissipation as the resolution increases. The turbulent transport

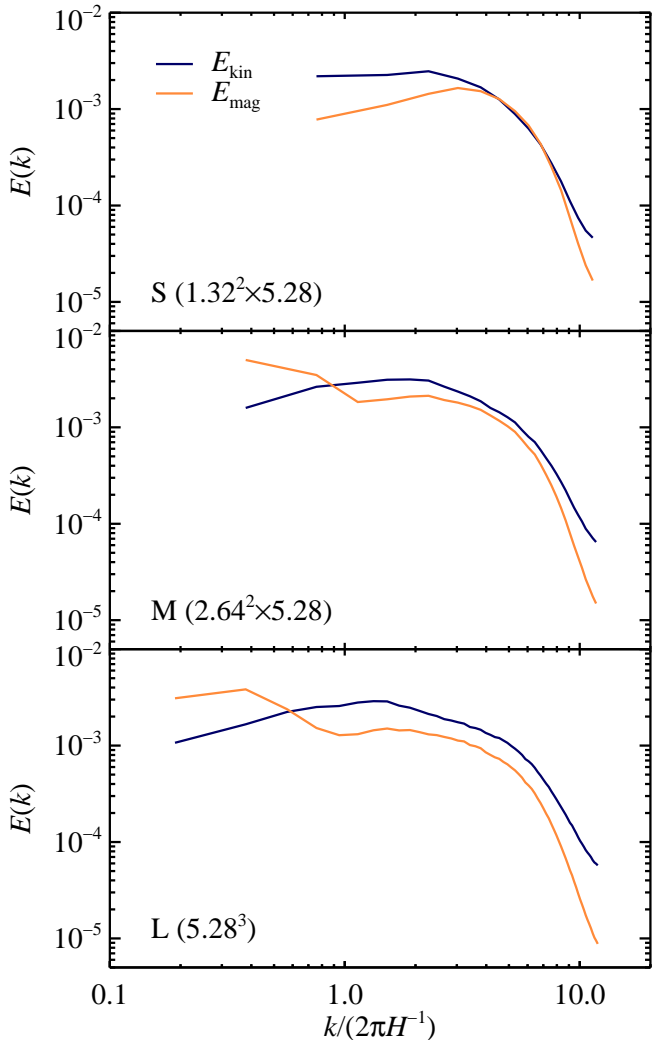


FIG. 2.— The kinetic (blue/dark) and magnetic (yellow/gray) energy spectrum, summed over shells of constant wavenumber $k = |\mathbf{k}|$. The kinetic energy dominates at the largest scales in the small box (top panel), whereas there is equipartition between kinetic and magnetic energy in a big range of smaller scales. In the two larger boxes (middle and bottom panels) the magnetic energy comes to dominate scales larger than approximately two scale heights. At the same time the equipartition at small scales is broken in favor of a dominance of kinetic energy.

coefficients in run M_{r2}, with twice as high resolution as run M, are approximately 50% lower than in run M (see Table 2). Such a linear scaling of transport coefficients with resolution extends the effect found by Fromang & Papaloizou (2007) to stratified boxes.

The kinetic and magnetic energy spectrum arising in boxes of different sizes is shown in Fig. 2, summed over wavenumber intervals $|\mathbf{k}| \in [k_{\text{cen}} - k_0/2, k_{\text{cen}} + k_0/2]$, with k_{cen} taking integer values times the smallest wavenumber k_0 . We have only included isotropic scales in the summation. Thus we exclude (a) long vertical wavelengths that exceed the radial or azimuthal extent of the smaller boxes in runs S and M, and (b) the anisotropic high wavenumbers which only exist in the “corners” of k -space. We averaged the energy spectra over 71 snapshots taken between 30 and 100 orbits.

For the two large runs (M and L) the kinetic energy (blue/dark) line dominates over magnetic energy

(yellow/gray) at scales below approximately $1 \dots 2$ scale heights. At larger scales (smaller k) the kinetic energy falls off gradually, whereas the magnetic energy keeps rising until finally peaking near the largest scales of the box. This transition from kinetically to magnetically dominated flow can only be seen when considering a sufficiently large box size. Interestingly the magnetic energy is comparable to kinetic energy near the dissipative sub-range in the smallest box, whereas the two energies move apart when the box size is increased.

In Fig. 3 we show for run L the spectral power of all dynamical components ($u_x, u_y, u_z, \rho, B_x, B_y, B_z$) as a function of radial wavenumber (x -axis), the smallest two azimuthal wavenumbers (columns) and the smallest three vertical wavenumbers (colored lines) in the first two columns. The third column, on the other hand, shows the spectral power as a function of vertical wavenumber, but for different, fixed values of the radial wavenumber. Looking first at the magnetic field (three bottom rows of Fig. 3) one sees that the radial and azimuthal magnetic energy peaks at the largest axisymmetric scales of the box ($k_y = 0$), whereas the non-axisymmetric modes have far less power. However, the large scale purely vertical modes shown in the third column contain approximately a factor four times more magnetic energy than the radial modes. The vertical component of the magnetic field has a rather flat dependence on all directions and show little large scale excitation.

The azimuthal velocity field component and the gas density also exhibit very high power at large axisymmetric scales; we return to those zonal flows in §4.

3.1. Magnetic Fields on Large Vertical Scales

The large scale power of the z -dependent radial and azimuthal magnetic field components, seen in the last column of Fig. 3, is illustrated in Fig. 4. In this figure we show the azimuthal magnetic field, averaged over the x and y directions, as a function of time t and height over the mid-plane z . Magnetic field structures propagate away from the mid-plane such that the field at a given height over the mid-plane flips signs at regular intervals. Similar buoyancy waves are seen in the simulations by Brandenburg et al. (1995), Miller & Stone (2000) and Hirose et al. (2006). The period of the sign flip is around 13 orbits, in agreement with the turbulent diffusion time-scale $t_D = H^2/\eta_t$, where $\eta_t \sim 0.01$ is the turbulent resistivity. This time is much longer than the correlation time of less than one orbit deduced in the previous section from the creation of azimuthal field from the radial field by the Keplerian stretching term.

The vertically propagating radial and vertical field may be the effect of a dynamo driven by rotation, stratification and shear (Parker 1955; Moffatt 1978). However, by correlating the mean field with the fluctuating electromotive force at both sides of the mid-plane, Brandenburg et al. (1995) concluded that the dynamo coefficient has the opposite sign of what is expected from mean field dynamo theory.

The non-stratified simulation L_{nogz} displays vertically dependent magnetic field structures propagating from and to the mid-plane. Without stratification there is no systematic helicity separation over the mid-plane, although patches of positive and negative helicity appear with a correlation time of a few orbits. The large-

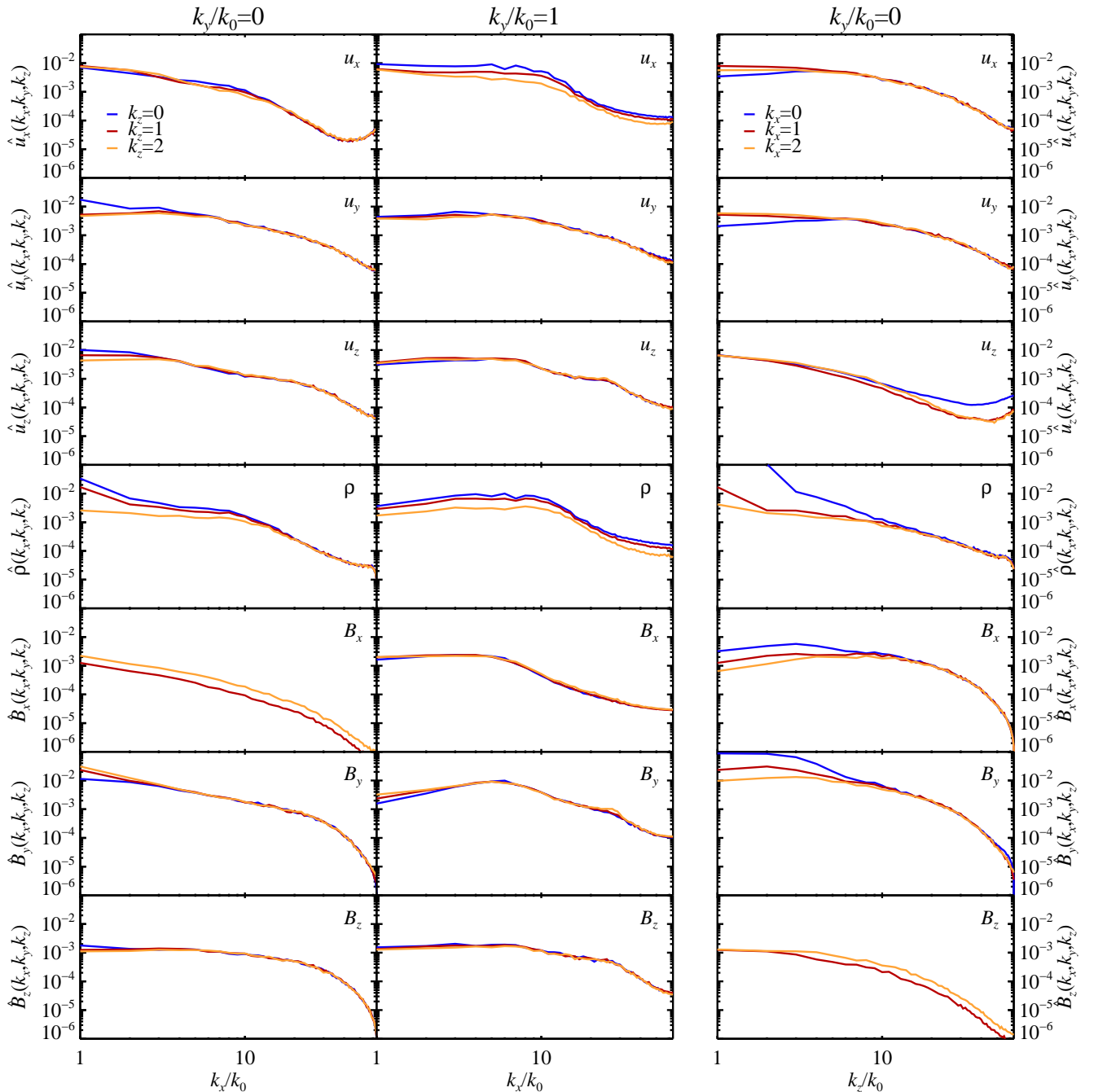


FIG. 3.— Fourier amplitudes of all dynamical variables for the stratified simulation with $L_x = L_y = L_z = 5.28H$, as a function of radial wavenumber k_x (two first columns) and vertical wavenumber k_z (last column). Colors indicate different wavenumbers in either the vertical direction (two first columns), or in the radial direction (last column), while the azimuthal wavenumber k_y is indicated at the top of each column. There is a clear tendency for u_x , u_y , ρ , B_x and B_y to peak at the largest radial scale of the box. However the last column shows that most large scale magnetic energy resides in modes with vertical variation. The variation of ρ with z is mainly due to the stratification.

scale magnetic field activity may come around as a result of an incoherent α - ω -dynamo (Vishniac & Brandenburg 1997), thriving on the fluctuating helicity, or be connected to magnetorotational instability in the azimuthal fields (Lesur & Ogilvie 2008).

4. ZONAL FLOWS

In Fig. 5 we show the gas density at the sides of the simulation box at $t = 72T_{\text{orb}}$ for run L (box size of $5.28H \times 5.28H \times 5.28H$). The turbulent structure of the gas density is clearly seen superimposed on the main

stratification in the left panel. The right panel shows the column density along each direction $\Sigma_i = \int \rho(x, y, z) dx_i$, divided by the directional column density in the initial stratification. There is a dominant column density structure at the largest radial scale of the box, with very little dependence in the azimuthal and vertical directions³.

The space-time plots of the gas density of runs S, M

³ The marked drop in column density near the upper and lower boundary planes is likely due to the periodic boundary conditions that precludes hydrostatic equilibrium near the boundaries by forcing the density derivative to be zero.

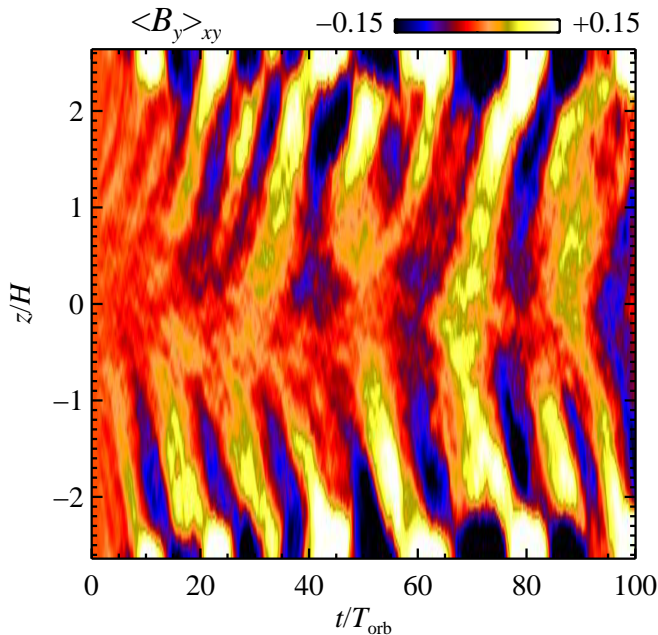


FIG. 4.— The azimuthal magnetic field B_y of run L as a function of time and height over the mid-plane. Field structures continuously propagate away from the mid-plane, causing the azimuthal field at a given height over the mid-plane to flip signs with a period of approximately 13 orbits.

and L shown in Fig. 6 confirm the dominance of the $k_x/k_0 = 1$ mode. Here we have averaged over the vertical and azimuthal directions and show the gas density as a function of radial coordinate x and time t measured in orbits. Both the density amplitude and the correlation time of the large scale structures increases significantly when making the box size larger. Run H is not shown in Fig. 6 – the long correlation time of the density structures in this huge box would require several hundred orbits integration to get good statistics.

Axisymmetric density modes have their power peak at the largest radial scale of the box. The azimuthal velocity has a similar peak at the largest axisymmetric modes (see Fig. 3). Fig. 7 compares the large-scale behavior of the density fluctuations to other physical quantities. Quantities are radially shifted so that the $k_x = k_0$ density bump peaks at the plot center, and then are time averaged. This filtering causes the plotted quantities (especially the gas density) to appear sinusoidal on the box scale, since higher order modes do not have a consistent phase relationship with the largest mode.

Fig. 7 shows an almost exact $-\pi/2$ phase difference between the radial peaks of the density and azimuthal velocity. This follows from near geostrophic balance between Coriolis forces and pressure,

$$2\rho_0\Omega u_y \approx \partial P/\partial x, \quad (12)$$

which gives super-Keplerian (sub-Keplerian) motions radially interior (exterior) to the density peak. In detail though the radial force balance includes Lorentz forces. The magnetic pressure and Maxwell stress perturbations in Fig. 7 are almost perfectly anti-correlated with the thermal pressure (the trend for thermal and magnetic pressures to misalign comes naturally out of the simplified zonal flow model presented in §5). This supports recent findings by T. Sano (personal communication,

2008).

Azimuthally and vertically varying modes have been averaged out of the density structures that appear in Fig. 6. But Fig. 3 shows that there is a clear trend for the density power to fall quickly with azimuthal wavenumber, likely because the Keplerian shear drives non-axisymmetric spectral power towards larger and larger k_x . The decreased spectral power of density at vertically varying modes can be seen as an effect of the Taylor-Proudman theorem. There is no geostrophic balance available for modes with vertical variation other than the main stratification, so pressure and turbulent diffusion will even out any vertical variation faster than the magnetorotational instability injects energy to those modes.

In Table 3 we show the measured values for the Fourier amplitudes of azimuthal velocity, density and Maxwell stress at the largest radial scale of the box, the power law index for the two largest radial scales, and the correlation time of the density structures. The power law index is found from

$$\zeta = \frac{\ln[|\hat{f}|(2k_0, 0, 0)] - \ln[|\hat{f}|(k_0, 0, 0)]}{\ln 2}. \quad (13)$$

We have normalized the density amplitude by the mean density in the box to get effectively the column density perturbation relative to the mean column density, $\hat{\rho}(k_0, 0, 0)/\langle \rho \rangle = \hat{\Sigma}(k_0, 0, 0)/\langle \Sigma \rangle$. The correlation time has been calculated by taking the value of ρ , averaged over y and z , at a given time t and measuring for each spatial point the time it takes for the density at that point to change by a value corresponding to the standard deviation of the gas density. The result has been averaged over many closely spaced times (for which the turbulence is saturated and the correlation time does not extend to the final time of the simulation) and multiplied by two to represent the full temporal extent of the correlated structures. The resulting correlation times are in good agreement with the life-time of the structures seen Fig. 6, and the measurements confirm the very long correlation times seen in simulation L. For the even larger box, simulation H, the correlation time is approximately 50 orbits, comparable to the total simulation time.

Interestingly the amplitude of the large scale azimuthal velocity is relatively independent of box size, while the density amplitude grows approximately proportional to the radial extent of the box⁴. There is an almost perfect geostrophic connection between the amplitude of the zonal flow and the normalized density amplitude, following the expected $|\hat{u}_y| \sim (1/2)k_0|\hat{\rho}|$. An exception to this is the mean vertical field runs (M_Bz.*) where the azimuthal velocity is higher than needed for geostrophic balance. We give a possible explanation for this discrepancy in §5.4, based on the relatively short correlation time of the turbulence in the imposed field runs.

The power law index of azimuthal velocity and density also follows the geostrophic expectation of $\zeta_\rho = \zeta_{u_y} - 1$, although both ζ_{u_y} and ζ_ρ decrease (towards zero) with increasing box size. This decrease could indicate some

⁴ Parceval's theorem would imply that the power at a given Fourier mode is inversely proportional to the number of grid points, but for the case of zonal flows, the power peaks so strongly at the largest radial mode that this reduction does not apply.

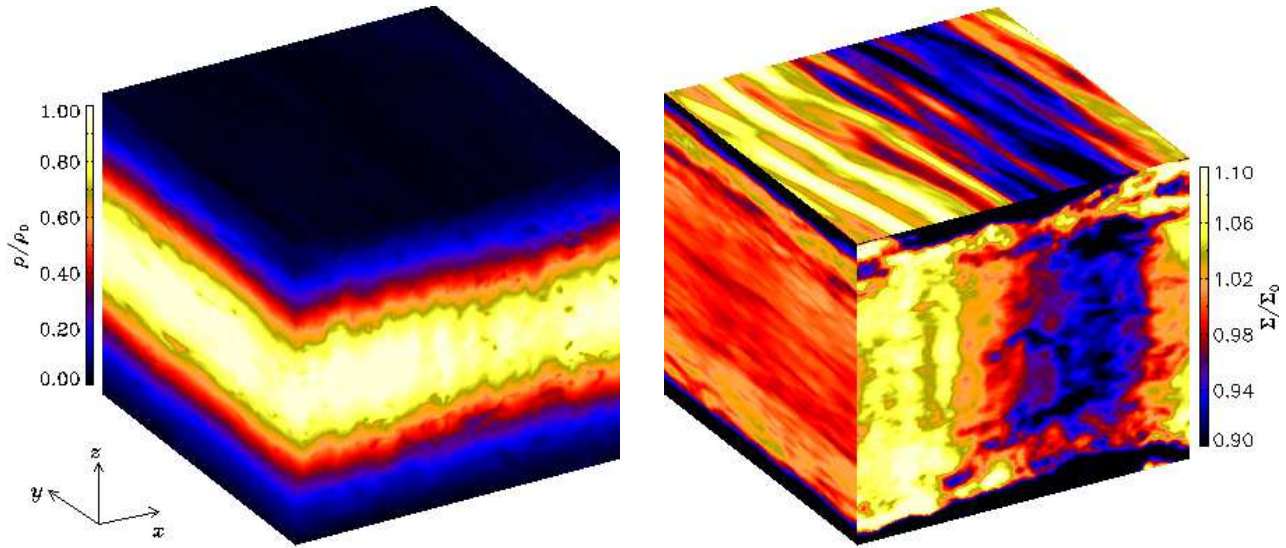


FIG. 5.— The gas density at the sides of the simulation box (left panel) and the directional column density (right panel, normalized by the column density of the original stratification) of run L at time $t = 72T_{\text{orb}}$. The dominant column density structure is vertically constant and axisymmetric and has variation mainly at the largest radial scale of the box.

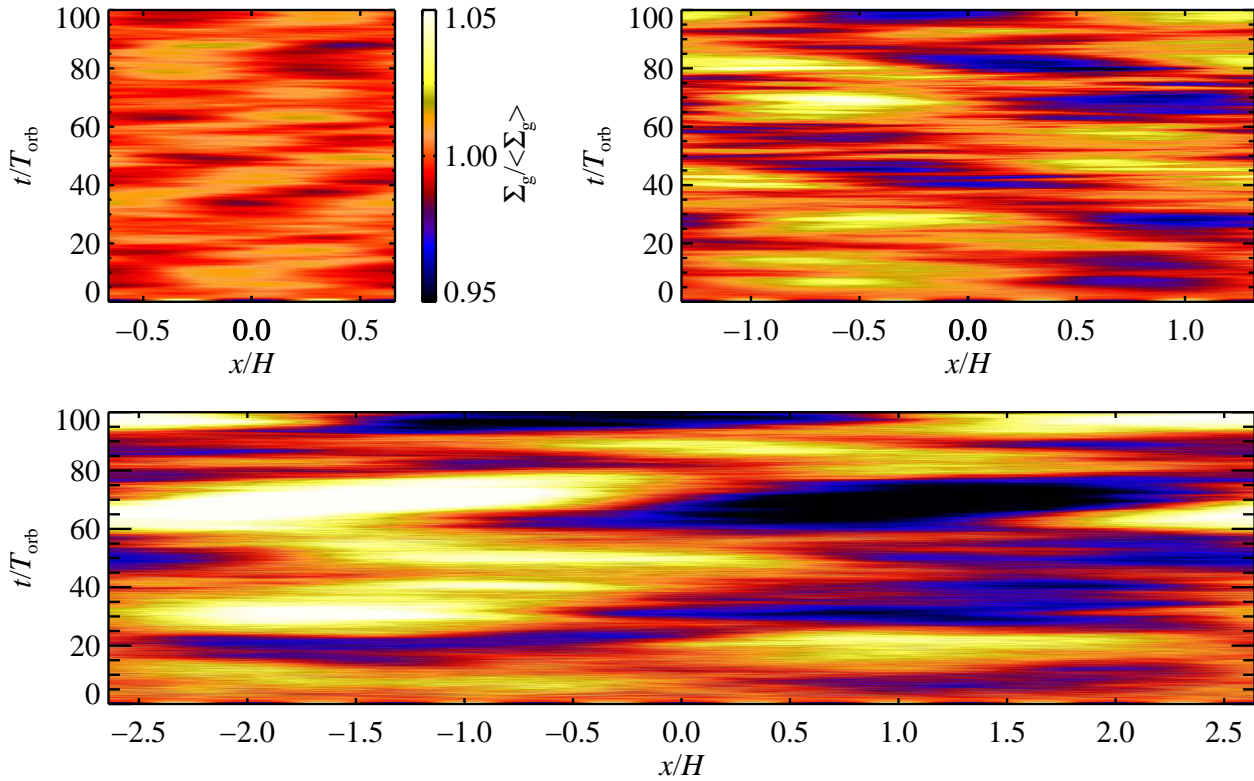


FIG. 6.— The gas density of runs S, M and L averaged over the y - and z -direction, as a function of radial distance from the center of the box, x , and the time, t , given in orbits. Density structures get higher amplitude and longer lived as the box size is increased from $L_x = L_y = 1.32H$ to $L_x = L_y = 5.28H$. The height of the box stays fixed at $L_z = 5.28H$.

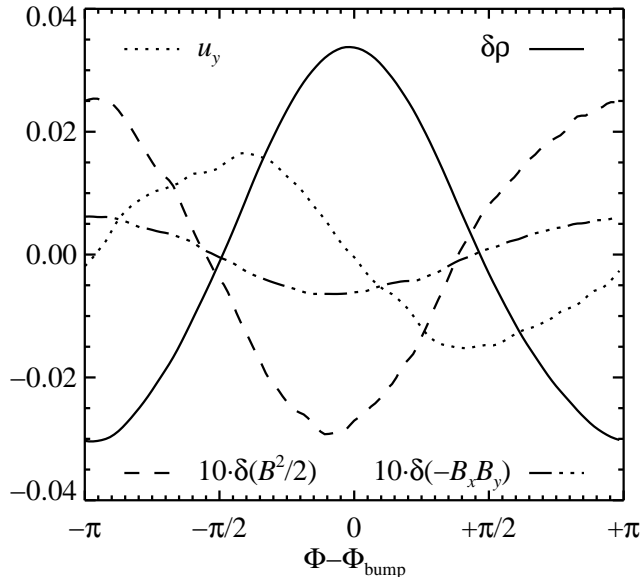


FIG. 7.— Phase-shifted and time-averaged perturbations to the gas density, azimuthal velocity, Maxwell stress (multiplied by 10 for visibility) and magnetic pressure (also multiplied by 10) for run L, as a function of the radial phase Φ . The $-\pi/2$ phase shift of u_y is a consequence of geostrophic balance on large scales. There is a clear anti-correlation of gas pressure (proportional to density) with Maxwell stress and magnetic pressure. Perturbations are azimuthally and vertically averaged for each time-step. Prior to time-averaging, the quantities are shifted in radius so that the lowest order radial perturbation (with $k_x = k_0 = 2\pi/L_x$) to the gas density is centered in the plot.

motion towards convergence of the zonal flow and pressure bumps. Global simulations will be needed to eventually find such convergence, since curvature effects could play an important role for simulation domains of more than ten scale heights.

The presence of large scale radial variation in Maxwell stresses is clear from Table 3. The amplitude is typically around 10–15% of the mean Maxwell stress, with a sharp decrease towards shorter wavelengths ($\zeta_{B_x B_y} \approx -1$). The imposed field simulations (M_BZ-*) even indicate an increasingly top heavy Maxwell stress with increasing resolution. However, the turbulence activity in that set of runs also increases by 50% as the resolution is increased (see Table 2), while the amplitude of the large scale Maxwell stress increases somewhat slower.

4.1. Large-Scale Balance

To get an understanding of the launching mechanism for zonal flows, we plot in Fig. 8 the energy balance of all vertically constant and axisymmetric modes. We have taken each term Q_i in the dynamical equation of variable f , $\hat{f} = \sum_i Q_i$, and calculated its contribution to the power of all the purely radial modes as

$$\frac{\partial |\hat{f}|^2}{\partial t} = \sum_i 2\text{Re}(\hat{f}^* \hat{Q}_i). \quad (14)$$

Here hats denotes Fourier transforms and stars complex conjugation. We add the power contribution from both the negative and the positive wavenumber in Fig. 8. The second panel of Fig. 8 indicates that the zonal flow [$\hat{u}_y(k_x)$] is excited primarily by the Lorentz force (indicated by the positive value of the “Lor” curve). A large

scale radial variation in the Maxwell stress (see Table 3 and §6) exerts a significant azimuthal tension on the gas. As the zonal flow is launched by the magnetic tension, the Coriolis force creates a slight radial component of the velocity field. The ensuing convergence of the gas flow creates the radial pressure bumps seen in Fig. 6 in perfect geostrophic balance between Coriolis force and pressure gradient force.

Fig. 9 shows that there is some correlation between the phase of the zonal flow and the phase of magnetic tension associated with the Maxwell stress, although the latter varies on a much shorter time-scale than the zonal flow. The magnetic tension is only an order of magnitude lower in amplitude than the saturated zonal flow, so a correlation time of the magnetic field of a few orbits is enough to explain the build up of large scale flow.

5. SIMPLIFIED MODEL OF ZONAL FLOWS

The zonal flows in our simulations have a very long correlation time, on the order of many tens of orbits. We can understand both the amplitude and the life-time of the zonal flows by adopting a simplified dynamical model which is forced by the azimuthal magnetic tension. Consider the following set of equations for the evolution of the radial velocity \hat{u}_x , azimuthal velocity \hat{u}_y and density $\hat{\rho}$, all for the large scale $\mathbf{k} = (k_0, 0, 0)$ mode,

$$0 = 2\Omega\hat{u}_y - \frac{c_s^2}{\rho_0}ik_0\hat{\rho}, \quad (15)$$

$$\frac{d\hat{u}_y}{dt} = -\frac{1}{2}\Omega\hat{u}_x + \hat{T}, \quad (16)$$

$$\frac{d\hat{\rho}}{dt} = -\rho_0 ik_0\hat{u}_x - \frac{1}{\tau_{\text{mix}}}\hat{\rho}. \quad (17)$$

Equation (15) expresses radial geostrophic balance⁵. We ignore for simplicity the role of Lorentz forces in this balance, evident from Fig. 8 to be an order unity correction. The azimuthal force balance in equation (16) describes forcing by the azimuthal tension \hat{T} , which is partly deflected into radial motion, but also directly accelerates the zonal flow in \hat{u}_y . Mass continuity in equation (17) includes a damping term with the timescale τ_{mix} . This represents non-linear advection terms, seen to be significant in Fig. 8 (bottom left panel). The same figure (top left and top center panels) shows that non-linear advection makes a negligible contribution to the momentum equations.

We can combine the above equations into a single evolution equation for the density,

$$\frac{d\hat{\rho}}{dt} = \frac{1}{1 + k_0^2 H^2} \left(\hat{F} - \frac{\hat{\rho}(t)}{\tau_{\text{mix}}} \right), \quad (18)$$

where $\hat{F} \equiv -2ik_0\rho_0\hat{T}/\Omega$ is the forcing term. The prefactor $c_k \equiv (1 + k_0^2 H^2)^{-1}$ is a pressure correction for small-scale modes that both decreases the amplitude of the forcing and increases the effective damping time. The density bump grows in exact antiphase with the stress bump \hat{S} , equivalent to the $\Sigma S = \text{const}$ relation of steady global accretion (Pringle 1981). This follows from writ-

⁵ Dropping $d\hat{u}_x/dt$ filters high frequency density waves which are not relevant for the longer-lived structures considered here.

TABLE 3
 ZONAL FLOW PROPERTIES

Run	$\langle -B_x B_y \rangle$	$ \hat{u}_y (k_0, 0, 0)$	$ \hat{\rho} (k_0, 0, 0)$	$ \widehat{B_x B_y} (k_0, 0, 0)$	ζ_{u_y}	ζ_ρ	$\zeta_{B_x B_y}$	t_{corr}
S	4.3×10^{-3}	1.9×10^{-2}	8.1×10^{-3}	4.5×10^{-4}	-1.6	-2.4	-0.9	8.3
M	1.2×10^{-2}	2.3×10^{-2}	1.9×10^{-2}	1.2×10^{-3}	-1.0	-1.8	-0.8	8.5
L	1.1×10^{-2}	1.7×10^{-2}	3.3×10^{-2}	1.3×10^{-3}	-1.0	-2.3	-1.4	19.6
H	1.0×10^{-2}	1.5×10^{-2}	5.2×10^{-2}	1.1×10^{-3}	-0.2	-1.1	-0.9	50.5
M_r2	6.5×10^{-3}	1.6×10^{-2}	1.3×10^{-2}	5.5×10^{-4}	-0.9	-2.2	-1.0	12.6
L_nogz	6.9×10^{-3}	1.2×10^{-2}	2.1×10^{-2}	5.6×10^{-4}	-0.8	-1.7	-1.0	18.8
M_Bz_r0.5	1.8×10^{-2}	4.5×10^{-2}	2.4×10^{-2}	2.1×10^{-3}	-1.1	-1.5	-0.6	4.6
M_Bz	2.5×10^{-2}	3.9×10^{-2}	2.4×10^{-2}	2.4×10^{-3}	-0.6	-1.9	-0.9	5.4
M_Bz_r2	2.7×10^{-2}	3.7×10^{-2}	1.8×10^{-2}	2.5×10^{-3}	-0.5	-1.5	-1.2	3.2
MS	5.2×10^{-3}	2.7×10^{-2}	2.3×10^{-2}	9.6×10^{-4}	-1.1	-1.5	-0.9	9.9
MS_r2	3.2×10^{-3}	1.5×10^{-2}	1.3×10^{-2}	4.0×10^{-4}	-0.8	-1.3	-0.8	11.3
MS_r2_fix	5.3×10^{-3}	2.9×10^{-2}	2.5×10^{-2}	7.7×10^{-4}	-0.9	-1.4	-0.5	15.7
SS_r4_nu1	2.8×10^{-3}	2.0×10^{-2}	8.5×10^{-3}	3.9×10^{-4}	-1.3	-2.1	-0.8	6.5
SS_r8_nu1	4.2×10^{-3}	2.2×10^{-2}	9.4×10^{-3}	5.4×10^{-4}	-1.5	-2.3	-0.9	7.6
MS_r4_nu1	6.8×10^{-3}	3.3×10^{-2}	2.8×10^{-2}	9.3×10^{-4}	-1.7	-2.4	-1.0	9.4

NOTE. — Col. (1): Name of run. Col. (2): Maxwell stress, normalized by mean pressure. Col. (3)-(5): Fourier amplitude of azimuthal velocity, density normalized by mean density in the box, and pressure-normalized Maxwell stress, respectively, at largest radial mode. Col. (6)-(8): Power law index of azimuthal velocity, density, and Maxwell stress, respectively, calculated from two largest radial modes. Col. (9): Correlation time, in orbits $T = 2\pi\Omega^{-1}$, of largest radial density mode.

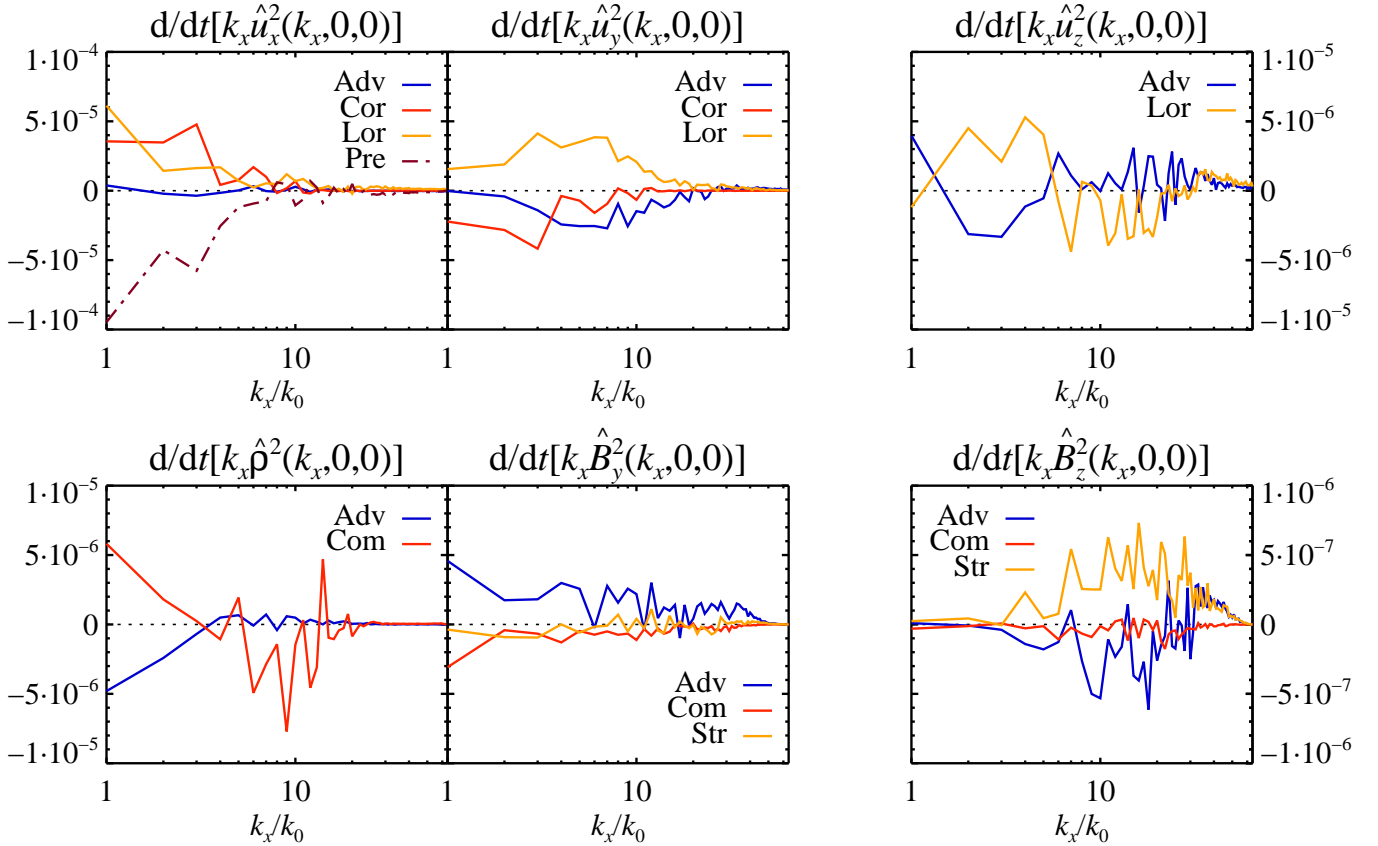


FIG. 8.— Power budget for all axisymmetric and vertically constant modes in run L. The curves show the power contribution from individual terms in the dynamical equations [“Adv”=advection, “Cor”=Coriolis force, “Lor”=Lorentz force, “Pre”=pressure gradient, “Com”=compression, “Str”=stretching]. The data has been averaged over equally spaced snapshots from $t = 30T_{\text{orb}}$ to $t = 100T_{\text{orb}}$ and multiplied by k_x for better visibility of the small scale power. The energy in the azimuthal velocity field (i.e. the zonal flow) is pumped by the Lorentz force (magnetic tension). The resulting convergence in the radial velocity leads to an increase in density amplitude and a decrease in azimuthal magnetic field. The compressive increase in gas density is in turn balanced by turbulent diffusion. The non-linear advection term in the induction equation for the azimuthal field, on the other hand, adds magnetic energy at the largest scale.

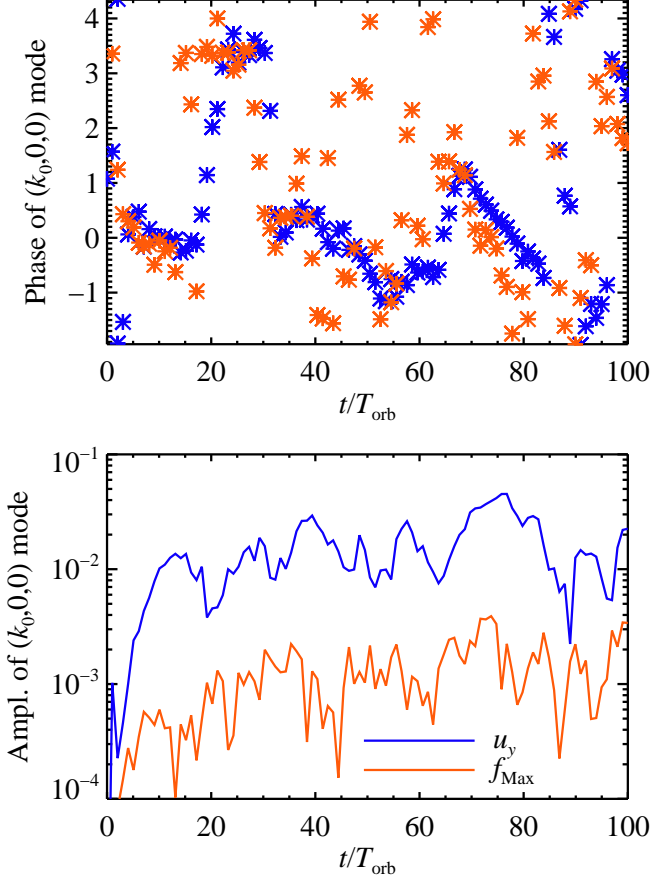


FIG. 9.— Phase and amplitude of the large-scale mode $(k_x, k_y, k_z)/k_0 = (1, 0, 0)$, for the azimuthal component of the velocity field and the magnetic tension associated with the Maxwell stress. There is some correlation between the phases (top panel), corroborating that zonal flows are indeed launched by the x -dependent Maxwell stress, although the Maxwell stress has variation on a much shorter time-scale than the zonal flows. The amplitude of the magnetic tension is approximately an order of magnitude smaller than the azimuthal velocity (bottom panel).

ing $\hat{F} = -2k_0^2\Omega^{-1}\hat{S}$, where the complex stress amplitude is defined as $\hat{S} = -\mu_0^{-1}\widehat{B_x B_y}$.

The straightforward equilibrium solution to equation (18) is $\hat{\rho}_{\text{eq}} = \tau_{\text{mix}}\hat{F}$. This is however not the correct solution to the problem since Fig. 9 clearly demonstrates that the magnetic tension forcing \hat{T} does not maintain a consistent phase relationship with \hat{u}_y (and thus with $\hat{\rho}$) during the life-time of a zonal flow.

Instead equation (18) should be modeled as a stochastic differential equation that gives the growth of the density and azimuthal velocity as a damped random walk. We now give a description of the approximate solution⁶. We assume that the forcing term $c_k\hat{F}$ has a correlation time τ_{for} . The density amplitude changes during each coherent step by $|\hat{\rho}_{\text{step}}| \sim c_k|\hat{F}|\tau_{\text{for}}$, and grows as a random

⁶ More formal solution methods exist as a manifestation of the fluctuation dissipation theorem. Youdin & Lithwick (2007) consider a mathematically similar problem: the stirring of particle velocities by aerodynamic coupling to turbulent gas. They show that the approximate arguments given here are consistent with more formal solutions to the stochastic Langevin equation via Fokker-Planck analysis.

walk, $\hat{\rho} \sim |\hat{\rho}_{\text{step}}|\sqrt{N_{\text{step}}} \sim |\hat{\rho}_{\text{step}}|\sqrt{t/\tau_{\text{for}}}$. The damping term sets the lifetime of coherent structures as

$$\tau_{\text{corr}} \sim \tau_{\text{mix}}/c_k \sim (1 + k_0^2 H^2)/(k_0^2 D_t), \quad (19)$$

where the final step describes the mixing process as diffusive with a strength D_t . The random walk saturates after $N_{\text{step}} \sim \tau_{\text{corr}}/\tau_{\text{for}}$ steps, resulting in the equilibrium value

$$\frac{\hat{\rho}_{\text{eq}}}{\rho_0} = 2\sqrt{c_k\tau_{\text{for}}\tau_{\text{mix}}}Hk_0\frac{\hat{T}}{c_s}. \quad (20)$$

We appeal to the simulations for appropriate values of \hat{T} , τ_{mix} and τ_{for} to check the consistency of the model. The forcing by magnetic tension can be estimated for run L from Fig. 9 to be approximately $\hat{T} \sim 0.001\Omega c_s$. From the same figure we read the correlation time of the forcing to be approximately $\tau_{\text{for}} \sim 10\Omega^{-1}$ (around two orbits). We assess the turbulent mixing time-scale as a diffusive process with $\tau_{\text{mix}} = 1/(k_0^2 D_t) \sim 70\Omega^{-1}$. Here we use $D_t \sim \alpha H^2\Omega \sim 0.01H^2\Omega$ for the turbulent diffusion coefficient.

With the above quantities, equation (20) gives an equilibrium density amplitude $\hat{\rho} \sim 0.041$ for run L, fairly close to the measured value $\hat{\rho} \sim 0.033$. This agreement is remarkable for such a simple model and actually a bit fortuitous, since Fig. 8 (top left panel) shows that radial Lorentz forces (neglected in this toy model) balance a significant portion of the pressure gradient, requiring a yet higher density perturbation.

5.1. Life-times of Pressure Bumps and Zonal Flows

Zonal flow lifetimes are a useful constraint on our understanding of large scale dynamics and mixing in MRI turbulence. The correlation times in Table 3 can be compared to the simple predictions of the random walk model in equation (19)⁷. In large shearing boxes, with $k_0 H \ll 1$, the lifetime increases with the diffusive mixing timescale, i.e. $t_{\text{corr}} \propto L_x^2$. For smaller boxes, with $k_0 H \gg 1$, the predicted t_{corr} is independent of box size for a fixed diffusion coefficient.

Indeed, $t_{\text{corr}} \approx 8 T_{\text{orb}}$ is nearly constant in the two smallest boxes, S and M, in rough agreement with the simple model. For runs L and H our estimate gives $t_{\text{corr}} \propto L_x^{1.23}$ in good agreement with measured value of $t_{\text{corr}} \propto L_x^{1.37}$ for these runs.

5.2. Consistency Checks on Forcing Model

We now check the consistency of our model further, first by computing the expected forcing timescale (the least well-measured quantity) in terms of better measured quantities. Inverting equation (20) gives

$$\tau_{\text{for}} \approx \left(\frac{\hat{\rho}}{2k_0 c_k \hat{T}}\right)^2 \frac{1}{\tau_{\text{corr}}}, \quad (21)$$

where we use $H = c_s = \rho_0 = 1$ and $\tau_{\text{corr}} = 2\pi\Omega t_{\text{corr}} = \tau_{\text{mix}}/c_k$. Since these are all known quantities (using $\hat{T} \propto k_0 \widehat{B_x B_y}$ normalized to $\hat{T} = 10^{-3}$ in run L), we compute $t_{\text{for}} = \tau_{\text{for}}/(2\pi) \approx \{0.64, 0.62, 1.5, 9.8\}$ orbits for runs {S,M,L,H}. That $t_{\text{for}} \ll t_{\text{corr}}$ supports the basic assumption of a random walk model.

⁷ Where $t_{\text{corr}} \equiv \tau_{\text{corr}}/(2\pi)$ since the former is in units of T_{orb} .

As another consistency check, we can measure the turbulent mixing coefficient, $D_t \equiv (\tau_{\text{mix}} k_0^2)^{-1}$ using the result from the random walk model that $2\pi t_{\text{corr}} \approx \tau_{\text{mix}}/c_k$. We get

$$D_t = \frac{1 + k_0^2}{2\pi t_{\text{corr}} k_0^2} \approx \{2.0, 2.2, 1.4, 1.2\} \times 10^{-2} \quad (22)$$

for runs {S,M,L,H}. The L and H runs give reasonable values, but the S and M runs have anomalously high mixing coefficients relative to other indicators of the strength of turbulence. However, the random walk model overall appears physically consistent and is useful in interpreting the simulations.

5.3. Extrapolation to scales $\gg H$

It is interesting to speculate how zonal flows would behave in even larger boxes than considered here. This is relevant in discs with aspect ratio $H/r \ll 0.1$, such as the discs around supermassive black holes in active galaxies (Frank et al. 2002; Goodman 2003).

Part of the observed growth in density amplitude with increasing box size is the corresponding increase of the c_k factor [eq. 20]. Since c_k tends towards unity with increasing wavelength, it will not contribute to the increase in $\hat{\rho}$ in boxes much larger than ten scale heights. Assuming further that τ_{for} and τ_{mix} scale approximately as $1/k_0^2$, and that $\hat{T} \propto k_0$, we predict that the density amplitude will not continue to grow, but will remain relatively constant on scales $\lambda \gg 10H$.

However, this prediction is uncertain, given that we do not have a full understanding of how the correlation time of the forcing depends on scale. Our analysis in the previous section indeed showed that τ_{for} grew faster than $1/k_0^2$ from box L to box H. Also it is not known whether $\overline{B_x B_y}$ will remain constant at very large scales. Instead the inverse cascade of magnetic energy may eventually terminate.

In larger boxes a wider range of scales can contribute to the density bumps, because of the long mixing time-scale, not just the largest scale that we considered above. This ‘‘oligarchic’’ regime may already have been reached in our run H ($L_x = 10.56H$) where the zonal flow amplitude is slightly smaller than in run L, while the zonal flow peaks much less strongly at the largest scale ($\zeta_{u_y} = -1.0$ for run L, but is only $\zeta_{u_y} = -0.2$ for run H).

5.4. Towards a More Complete Theory

A more complete theory of large scale dynamics would include the self-consistent evolution of magnetic fields. For instance, the magnetic pressure grows from the Maxwell stress, via the term

$$\frac{\partial[(1/2)B_y^2]}{\partial t} = \dots - \frac{3}{2}\Omega B_x B_y, \quad (23)$$

which readily follows from the induction equation (3). Thus the magnetic pressure grows in regions of stronger (more negative) Maxwell stress. The density, on the other hand decreases in regions of high stress. Fig. 7 clearly shows the anticorrelation of density (and thus thermal pressure) with both Maxwell stresses and magnetic pressure. Though not shown in the plot, actually

all components of the magnetic pressure are found to be lower in the density peak.

The departure from geostrophic balance for the imposed field runs M_Bz_* likely arises from the relatively short correlation time of the more vigorous turbulence in these simulations. This can break the validity of equation (15) by launching density waves. From equations (16) and (17) we see that zonal flows can be launched immediately by the magnetic tension ($d\hat{u}_y/dt = \hat{T}$), without leaking into the Coriolis force ($-\Omega u_x/2$) that gives radial compression. This way a pressure bump does not have enough time to react to the zonal flow before the magnetic tension shifts position.

The recent work by Vishniac (2008) offers a model for the growth of large scale structures in MRI turbulence, including an induction equation for field evolution. Other features which differ from our model include incompressibility and the neglect of azimuthal accelerations (while we ignored radial ones). Most important, Vishniac (2008) considers only disturbances with a sinusoidal vertical dependence, which leads to the growth of vertically varying rolls. The relation between these structures and the height-independent zonal flows that emerge from our model deserves further study.

6. INVERSE CASCADE

So far we have shown that the large scale variation in the Maxwell stress launches slightly compressive zonal flows, which in turn enter geostrophic balance with axisymmetric column density bumps.

The magnetic energy in the azimuthal field is pumped to the largest radial scales of the box by the advection term (in the induction equation, see Fig. 8). This inverse cascade is also evident from Fig. 10. Here we plot the power contribution from different terms in the induction equation to the magnetic field, summing over shells of constant wavenumber and averaging over equally spaced snapshots during the saturated state of run L. The radial and azimuthal field both get a net positive contribution from the advection term at large scales, whereas the magnetic stretching term (including stretching by the background shear) adds energy with a peak at middle scales around $k/k_0 \sim 20$. The source B_x for Keplerian stretching is itself generated by non-Keplerian stretching at both moderate and small scales. For the vertical field component Fig. 10 shows no sign of large scale magnetic energy activity. This is interesting in connection with a possible accretion disk dynamo, because the lack of large scale activity of B_z may indicate that vertical field, crucial for the vertical field MRI to operate, is only replenished at scales near the dissipative subrange of the turbulence, but not on the large scales. Azimuthal fields are unstable to a non-axisymmetric magnetorotational swing instability (Balbus & Hawley 1992), which has a significant growth rate at short vertical wavelengths (Foglizzo & Tagger 1995; Terquem & Papaloizou 1996). Fig. 10 indicates that the azimuthal field is actively processing energy, through the various terms in the induction equation, even at the largest scales of the box.

Fig. 10 also shows that compression is a sink of magnetic energy at the largest scales, for both radial and azimuthal field. The zonal flow launched by the radially dependent Maxwell stress indeed creates a diverging velocity field in regions where the magnetic field is high,

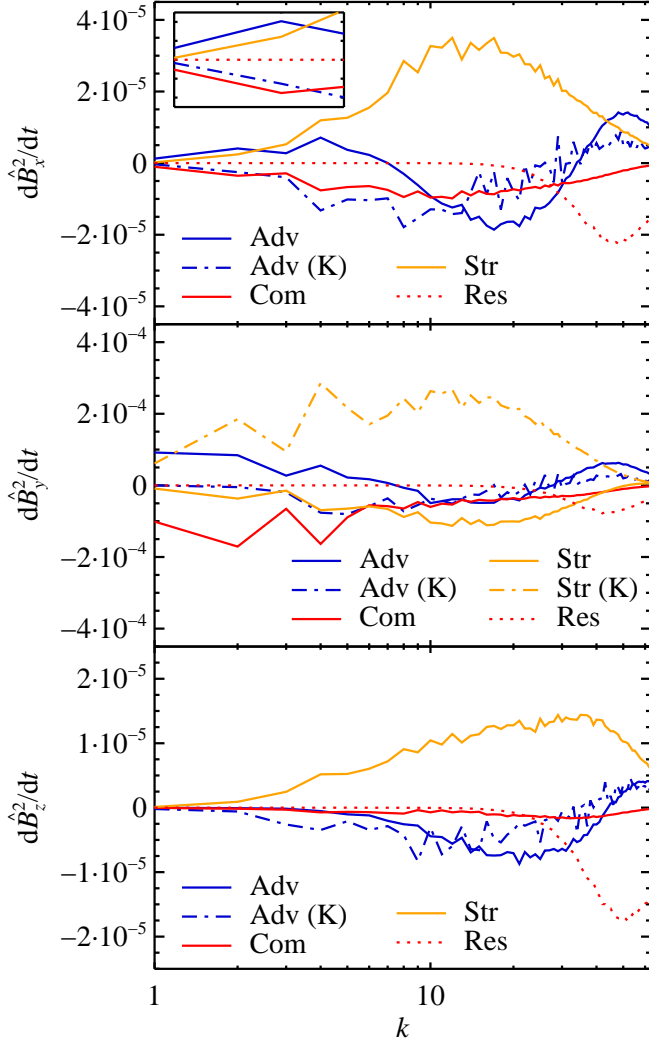


FIG. 10.— Contribution from different terms of the induction equation to the magnetic energy at scale k , summed over shells of constant $k = |\mathbf{k}|$, including the contribution from the hyperresistivity [“Res”]. Both the x - and y -components of the magnetic field get a positive energy injection at the largest scale from the advection term [“Adv”]. Another important energy source is the Keplerian stretching term [“Str (K)”]. The regular stretching term ([“Str”]) injects energy at all scales of B_x and B_z , but is an energy sink for B_y .

lowering the magnetic energy at the largest scales. This way the zonal flows are self-limiting, as they reduce the large scale variation in the magnetic field.

When the magnetic energy in the radial field component cascades up to the largest scales of the box, then the Maxwell stress at those scales can grow through the negative definite Keplerian stretching term,

$$\partial(B_x B_y)/\partial t = \dots - (3/2)\Omega B_x^2. \quad (24)$$

The deepest source of the zonal flows thus lies primarily in the inverse cascade of the radial magnetic field energy. In Fig. 11 we show the radial magnetic energy and the Maxwell stress in run L, averaged over the azimuthal and vertical directions and normalized by the instantaneous mean. There is an astonishing correlation between the two quantities.

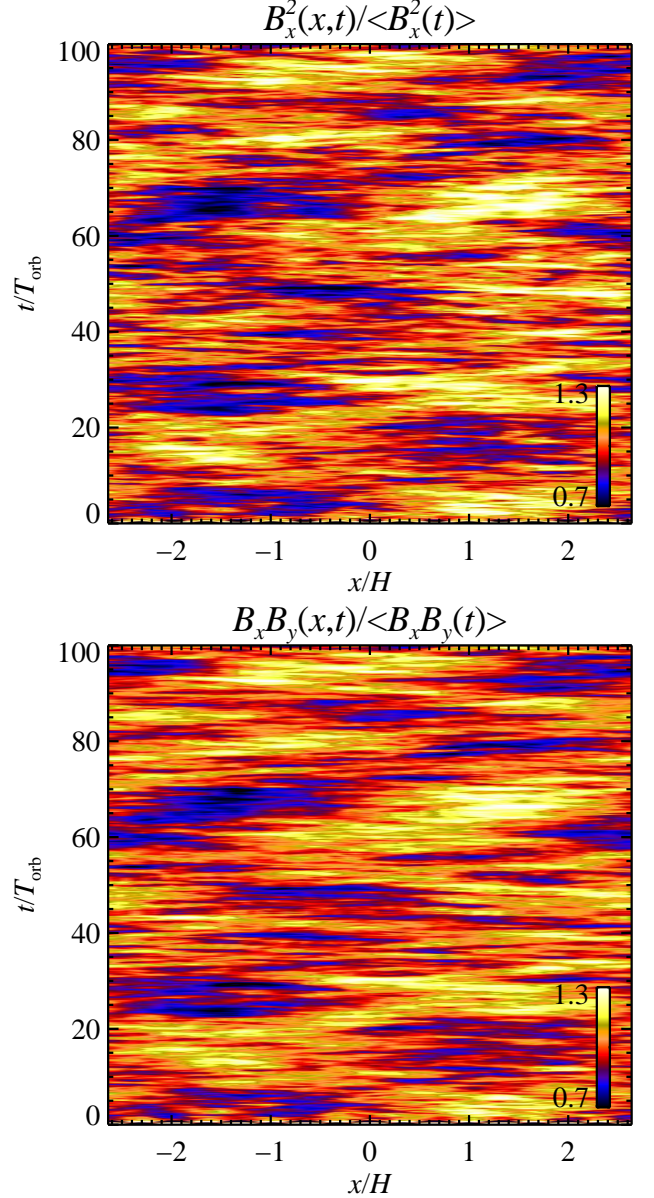


FIG. 11.— The radial magnetic energy (top panel) and the Maxwell stress (bottom panel) in run L, both averaged over the azimuthal and vertical directions and normalized by the instantaneous mean. There is an almost perfect correlation between the two quantities, arising from Keplerian stretching of the radial magnetic field. Energy and stress fluctuations peak at 30% of the mean value, but the average fluctuation is only around 10%. The coherence time is generally a few orbits, with periods of coherence times up to ten orbits. The correlation time of the density structures shown in Fig. 6 is much longer.

6.1. Hydrodynamical Inverse Cascade?

The slightly positive energy contribution of the advection term to the velocity field (Fig. 8) represents evidence for an additional inverse cascade for the azimuthal velocity. Such an inverse cascade occurs commonly in 2-D turbulence (Kraichnan 1967; Borue 1993) and in 3-D rotating turbulence (e.g. Bartello et al. 1994; Cambon et al. 1997). In the latter case vertically symmetric cyclones and anticyclones emerge at scales large enough for Coriolis forces to dominate (i.e. Rossby number $Ro \ll 1$). Cascade of small scale turbulent energy to large scale Rossby waves and zonal jets in protoplanetary discs was

proposed by Sheehan et al. (1999). However, in our simulations the hydrodynamical inverse cascade is found to give a more than 10 times smaller contribution to the large scale kinetic energy than the variation in Maxwell stress and magnetic energy do.

7. NUMERICAL ISSUES AND VALIDATION TESTS

Supersonic shear flow in large shearing boxes introduces a space-dependent numerical dissipation which can lead to artificial suppression of turbulence near the edges of the box (Johnson et al. 2008). In this section we present various tests to validate the results of the non-linear simulations.

7.1. Results for Various Shearing Box Algorithms

In Appendix C we show variations of runs S–H where we use several different ways to solve the shearing box equations. The various schemes – FDA (Finite Difference Advection), RRC (Random Revolution Center), SRD (Systematic Radial Displacement), and SAFI (Shear Advection by Fourier Interpolation) – are discussed in detail in Appendix C. The statistical properties of the zonal flows and the pressure bumps are given in Table 4. The large scale variation in the Maxwell stress remains at around 10% of the mean Maxwell stress, independent of the shearing box algorithm. The amplitudes of azimuthal velocity and density, on the other hand, are clearly larger when applying the straightforward finite difference advection scheme, indicating that this scheme artificially enhances the correlation time of the Maxwell stress. For the standard finite difference advection scheme of the Pencil Code we furthermore observe a tendency for turbulence to be weaker near the edge of the box and for the largest radial density mode to have its minimum near the center of the box (see Fig. 16 of Appendix C) for the two largest boxes, confirming the results of Johnson et al. (2008). However, with the two improved shearing box algorithms Systematic Radial Displacement (SRD) and Shear Advection by Fourier Advection (SAFI), any consistent preference for stronger turbulence near the box center is no longer present. This was our primary reason for presenting the SAFI versions of L and H in the main text.

7.2. Convergence Tests

To quantify the effect of dissipation parameters and grid resolution on the amplitude of zonal flows and on the inverse cascade of magnetic energy we run two sets of simulations: (a) runs M_Bz at three different resolutions with decreasing diffusivity coefficients and (b) runs MS at two different resolutions, the higher resolution simulations run both with a fixed and with a decreased diffusivity. The results are given in Table 2 and Table 3.

For the imposed field simulations M_Bz there is an overall increase in the turbulent activity of 50% when going from the lowest (M_Bz_r0.5) to the highest resolution (M_Bz_r2), while the zonal flow and the density bumps decrease by around 20% in amplitude. In this series of runs we have decreased the hyperdiffusivity coefficients proportional to δx^5 with increasing resolution. The increase in turbulent stresses may thus be due to the ever larger inertial range. At the same time these added scales will act as an increased diffusivity on the

large scale pressure bumps, so it is not surprising that the zonal flows fall slightly in amplitude.

The MS series of runs are non-stratified and have a computational domain of $L_x = L_y = 2.64H$ and $L_z = 1.32H$. For the low resolution simulation (MS) we have forced a time-step similar to that of the higher resolution run (MS_r2_fix), to have approximately the same amount of numerical dissipation, and we apply the Systematic Radial Displacement scheme described in Appendix C to ensure that the numerical dissipation does not have significant dependence on x . We find that zonal flows decrease in amplitude when increasing the resolution while keeping the *mesh* hyper-Reynolds number constant (compare run MS to run MS_r2 in Table 3). The mesh hyper-Reynolds number is here defined as $Re_3 = \max(u)\delta x^5/\nu_3$. However, the overall turbulent activity also falls significantly as the resolution is increased, so the reduction in the large scale amplitudes may simply be due to the decrease in available power at the small scales. On the other hand if dissipation parameters are kept constant as the resolution is increased (as in run MS_r2_fix), then there is little or no effect on turbulent activity and on zonal flow/pressure bump statistics. It is encouraging that extra spatial resolution has so little effect on the turbulent state when the dissipation, and thus spectral range, is held fixed. Ultimately even higher resolution simulations will be needed to fully discern the effect of scale separation and Reynolds numbers on the zonal flow amplitude.

7.3. Laplacian Dissipation

The simulations we have presented so far all used hyperdiffusivity operators to dissipate energy near the smallest scales of the simulation. This is a “trick” that allows us to extend the inertial range of the turbulence, at the cost of a steeper transition into the dissipative subrange. To check that the use of hyperdiffusivity does not create any spurious flows, we have run three simulations using regular Laplacian operators for viscosity and resistivity (runs SS_r4_nu1, SS_r8_nu1, and MS_r4_nu1). In order to ensure that the box can sustain turbulence, we set the magnetic Prandtl number (defined as ratio of viscosity coefficient ν_1 to resistivity coefficient η_1) to approximately $Pm \equiv \nu_1/\eta_1 = 4$ (following Fromang et al. 2007, who found that turbulence in zero net flux boxes without stratification is generally only sustained when $Pm > 1$). Still the Pencil Code only showed sustained turbulence at a resolution of at least 100 grid points per scale height, as lower resolution would either show decaying turbulence at low magnetic Reynolds numbers, or crash due to lack of dissipation at high magnetic Reynolds numbers.

For moderate and high resolutions, the results in Table 2 and Table 3 show that the Laplacian simulations exhibited fairly strong turbulence with just as strong zonal flows as the hyperdiffusivity runs. This yields much support to the fact that the zonal flows are real, and not a numerical artifact, because of the more physical nature of the Laplacian operators and the fact that zonal flows operate also at 200 grid points per scale height in resolution, a factor eight times higher resolution than the hyperdiffusivity runs S–H. However there is a significant increase in turbulent activity when going from run SS_r4 to run SS_r8. The fact that the MRI has not yet con-

TABLE 4
ZONAL FLOW PROPERTIES FOR VARIOUS SHEARING BOX SCHEMES

Run	$\langle -B_x B_y \rangle$	$ \hat{u}_y (k_0, 0, 0)$	$ \hat{\rho} (k_0, 0, 0)$	$ \widehat{B_x B_y} (k_0, 0, 0)$	ζ_{u_y}	ζ_ρ	$\zeta_{B_x B_y}$	t_{corr}
S (FDA)	4.2×10^{-3}	1.9×10^{-2}	8.1×10^{-3}	4.5×10^{-4}	-1.6	-2.4	-0.9	8.3
S (RRC)	2.3×10^{-3}	1.8×10^{-2}	8.0×10^{-3}	2.7×10^{-4}	-1.5	-2.4	-0.7	14.9
S (SRD)	3.1×10^{-3}	1.8×10^{-2}	7.9×10^{-3}	3.8×10^{-4}	-1.5	-2.3	-0.8	8.9
S (SAFI)	2.8×10^{-3}	1.8×10^{-2}	8.1×10^{-3}	3.7×10^{-4}	-1.5	-2.5	-0.8	12.3
M (FDA)	1.2×10^{-2}	2.4×10^{-2}	1.9×10^{-2}	1.2×10^{-3}	-1.1	-1.8	-0.7	8.5
M (RRC)	8.6×10^{-3}	2.6×10^{-2}	2.4×10^{-2}	9.7×10^{-4}	-1.3	-2.3	-1.0	11.6
M (SRD)	8.8×10^{-3}	1.7×10^{-2}	1.7×10^{-2}	8.7×10^{-4}	-0.5	-1.8	-0.8	8.3
M (SAFI)	9.6×10^{-3}	1.9×10^{-2}	1.6×10^{-2}	9.2×10^{-4}	-0.8	-1.8	-0.7	8.4
L (FDA)	1.1×10^{-2}	2.5×10^{-2}	5.0×10^{-2}	1.3×10^{-3}	-1.1	-2.3	-1.0	18.6
L (RRC)	1.3×10^{-2}	1.8×10^{-2}	3.6×10^{-2}	1.1×10^{-3}	-0.5	-1.6	-0.5	20.1
L (SRD)	1.1×10^{-2}	2.0×10^{-2}	4.0×10^{-2}	1.2×10^{-3}	-0.6	-1.9	-0.9	20.9
L (SAFI)	1.1×10^{-2}	1.7×10^{-2}	3.3×10^{-2}	1.3×10^{-3}	-1.0	-2.3	-1.4	19.6
H (FDA)	9.5×10^{-3}	1.6×10^{-2}	5.8×10^{-2}	1.1×10^{-3}	-0.4	-1.4	-1.1	57.1
H (SAFI)	1.0×10^{-2}	1.5×10^{-2}	5.2×10^{-2}	1.1×10^{-3}	-0.2	-1.1	-0.9	50.5

NOTE. — Col. (1): Name of run. Col. (2): Maxwell stress, normalized by mean pressure. Col. (3)-(5): Fourier amplitude of azimuthal velocity, density normalized by mean density in the box, and pressure-normalized Maxwell stress, respectively, at largest radial mode. Col. (6)-(8): Power law index of azimuthal velocity, density, and Maxwell stress, respectively, calculated from two largest radial modes. Col. (9): Correlation time, in orbits $T = 2\pi\Omega^{-1}$, of largest radial density mode. The various shearing box algorithms – FDA, RRC, SRD, and SAFI – are defined in Appendix C.

verged even at such high resolution is a slight worry. It may indicate either that numerical dissipation still influences the saturation level of the turbulence or that the introduction of smaller scales changes the dynamics of the system. One would hope that the MRI will converge at the next resolution level, i.e. 400 grid points per scale height, but this huge computational effort is beyond the scope of the current investigation. The ratio of the large scale Maxwell stress variation to the mean value nevertheless stays approximately the same for the two runs SS_r4 and SS_r8, indicating some convergence in the inverse cascade of magnetic energy.

8. SUMMARY AND DISCUSSION

We conduct numerical simulations of turbulence driven by the magnetorotational instability (MRI) in large shearing boxes. We here emphasize four main results. (1) The turbulent energy and stresses more than double when the box size (radial and azimuthal) increases from 1.32 to 2.64 scale heights. In yet larger boxes the turbulent fluctuations and stresses remain relatively constant. (2) Magnetic energy exceeds kinetic energy by a factor two-three on scales above approximately two scale heights, when the box size is sufficient for the inverse case to proceed to these large scales. (3) Axisymmetric surface density fluctuations grow to fill the box, and persist for many orbits, with an increasing lifetime in bigger boxes. These pressure bumps are in geostrophic balance with sub/super-Keplerian zonal flows. (4) We put forward a simple model for the launching of zonal flows by large scale variations in the Maxwell stress. This random walk model explains both the saturated amplitude as well as the correlation time of pressure bumps and their associated zonal flows.

Large scale pressure and zonal flow structures grow to fill the simulation domain for all box sizes. The largest box size considered, more than ten scale heights in radial and azimuthal extent, nevertheless indicates an in-

creasingly flat dependence of zonal flow power on the radial wave number. Even larger simulation domains will be needed to verify whether the natural scale of the large scale structures is really around ten scale heights. Global effects – including curvature and radial variation in background quantities like density and sound speed – may also play a vital role for the termination of the inverse cascade. The global simulations by Lyra et al. (2008) show evidence of long lived radial pressure bumps that have not cascaded to the largest radial scale of the disk (see their Fig. 18). It is intriguing to note that the length scale of the pressure bumps in Lyra et al. (2008) is around ten scale heights.

We have experimented with several improvements of the shearing box algorithm in order to quantify the dependence of the results on numerical diffusivity associated with the Keplerian shear flow. There is a tendency for the density depression to occur at the center of the box for the two largest box sizes (approximately five and ten scale heights in radial extent, respectively) if shear advection is done by the usual finite difference scheme of the Pencil Code, confirming a similar effect found by Johnson et al. (2008) for a ZEUS-like code (Stone & Norman 1992). However, when shear advection is integrated by high order interpolation instead, we see no preference for any special location in the box. The same is true if the state of the gas is displaced systematically by one grid point in the radial direction at the beginning of each time-step.

Ultimately the emergence of zonal flows and pressure bumps is controlled by the large scale variation of the magnetic field. The cascade of magnetic energy from small to large scales only occurs for the x - and y -components of the field. The vertical field, which is of importance for feeding the vertical field MRI, shows very little large scale behavior. The specific mechanism that leads to the inverse cascade of the in-plane field in our simulations is not known. In the absence of any net ki-

netic helicity separation in the radial direction, the large scale field may arise as an effect of a negative turbulent diffusivity (e.g. Zheligovsky et al. 2001; Urpin 2002) or a shear current effect (Rogachevskii & Kleeorin 2003; Yousef et al. 2008).

Both hyperdiffusivity simulations and direct numerical simulations (DNS), with Laplacian viscosity and resistivity operators, show prodigious zonal flows. A fruitful future path could be to focus on even higher resolution direct simulations of resistive MRI turbulence. This could probe the dependence of the inverse cascade of magnetic energy and the launching of zonal flows on the magnetic Reynolds number and the Prandtl number (Lesur & Longaretti 2007; Fromang et al. 2007), believed to be much smaller than unity in most parts of accretion disks (Balbus & Henri 2008).

Our numerical experiments show that the magnetic field takes particular advantage of larger spatial scales

by participating in an inverse cascade. This in turn produces long-lived density fluctuations which can have significant influence on the formation and evolution of planetary systems. Big shearing boxes thus provide an excellent tool for studying turbulent accretion disks and the physical processes that occur therein.

We are grateful to Takayoshi Sano, Ethan Vishniac, Axel Brandenburg, Eric Blackman, Yuri Levin and Wladimir Lyra for inspiring discussions on large scale magnetic fields in accretion disks. We would like to thank the anonymous referee for an insightful referee report. Bryan Johnson is thanked for commenting an early version of the manuscript. H. K. has been supported in part by the Deutsche Forschungsgemeinschaft DFG through grant DFG Forschergruppe 759 “The Formation of Planets: The Critical First Growth Phase”.

REFERENCES

- Arlt, R., & Rüdiger, G. 2001, *A&A*, 374, 1035
 Armitage, P. J. 1998, *ApJ*, 501, L189+
 Balbus, S. A., & Hawley, J. F. 1991, *ApJ*, 376, 21
 Balbus, S. A., & Hawley, J. F. 1992, *ApJ*, 400, 610
 Balbus, S. A., & Hawley, J. F. 1998, *Reviews of Modern Physics*, 70, 1
 Balbus, S. A., & Hawley, J. F. 2006, *ApJ*, 652, 1020
 Balbus, S. A., & Henri, P. 2008, *ApJ*, 674, 408
 Bartello, P., Metais, O., & Lesieur, M. 1994, *Journal of Fluid Mechanics*, 273, 1
 Blum, J., & Wurm, G. 2008, *ARA&A*, 46, 21
 Borue, V. 1993, *Physical Review Letters*, 71, 3967
 Brandenburg, A., Nordlund, Å., Stein, R.F., & Torkelsson, U. 1995, *ApJ*, 446, 741
 Brandenburg, A. 2003, in *Advances in nonlinear dynamos (The Fluid Mechanics of Astrophysics and Geophysics, Vol. 9)*, ed. A. Ferriz-Mas & M. Núñez (Taylor & Francis, London and New York), 269-344
 Brandenburg, A., & Subramanian, K. 2005, *Phys. Rep.*, 417, 1
 Brauer, F., Dullemond, C. P., & Henning, T. 2008, *A&A*, 480, 859
 Brauer, F., Henning, T., & Dullemond, C. P. 2008, *A&A*, 487, L1
 Busse, F. H. 1976, *Icarus*, 29, 255
 Cambon, C., Mansour, N. N., & Godeferd, F. S. 1997, *Journal of Fluid Mechanics*, 337, 303
 Diamond, P. H., Itoh, S.-I., Itoh, K., & Hahm, T. S. 2005, *Plasma Physics and Controlled Fusion*, 47, 35
 Dominik, C., Blum, J., Cuzzi, J. N., & Wurm, G. 2007, in *Protostars and Planets V*, ed. B. Reipurth, D. Jewitt, & K. Keil, 783-800
 Dullemond, C. P., & Dominik, C. 2005, *A&A*, 434, 971
 Foglizzo, T., & Tagger, M. 1995, *A&A*, 301, 293
 Frank, J., King, A., & Raine, D. J. 2002, *Accretion Power in Astrophysics: Third Edition* (Cambridge University Press, 2002)
 Fromang, S., & Nelson, R. P. 2005, *MNRAS*, 364, L81
 Fromang, S., & Nelson, R. P. 2006, *A&A*, 457, 343
 Fromang, S., & Papaloizou, J. 2007, *A&A*, 476, 1113
 Fromang, S., Papaloizou, J., Lesur, G., & Heinemann, T. 2007, *A&A*, 476, 1123
 Gammie, C. F. 2001, *ApJ*, 553, 174
 Goodman, J. 2003, *MNRAS*, 339, 937
 Haghhighipour, N., & Boss, A. P. 2003, *ApJ*, 583, 996
 Haugen, N. E., & Brandenburg, A. 2004, *Phys. Rev. E*, 70, 036408
 Hawley, J. F., Gammie, C. F., & Balbus, S. A. 1995, *ApJ*, 440, 742
 Heimpel, M., & Aurnou, J. 2007, *Icarus*, 187, 540
 Hirose, S., Krolik, J. H., & Stone, J. M. 2006, *ApJ*, 640, 901
 Howard, R., & Labonte, B. J. 1980, *ApJ*, 239, L33
 Ida, S., Guillot, T., & Morbidelli, A. 2008, *ApJ*, 686, 1292
 Johansen, A., & Klahr, H. 2005, *ApJ*, 634, 1353
 Johansen, A., Klahr, H., Henning, Th. 2006, *ApJ*, 636, 1121
 Johansen, A., Oishi, J. S., Low, M.-M. M., Klahr, H., Henning, T., & Youdin, A. 2007, *Nature*, 448, 1022
 Johansen, A., Brauer, F., Dullemond, C., Klahr, H., & Henning, T. 2008, *A&A*, 486, 597
 Johnson, E. T., Goodman, J., & Menou, K. 2006, *ApJ*, 647, 1413
 Johnson, B. M. 2007, *ApJ*, 660, 1375
 Johnson, B. M., Guan, X., & Gammie, C. F. 2008, *ApJS*, 177, 373
 Kato, M. T., Nakamura, K., Tandonoro, R., Fujimoto, M., & Ida, S. 2008, *ArXiv e-prints*, 0810.3466
 Klahr, H., & Lin, D. N. C. 2001, *ApJ*, 554, 1095
 Kraichnan, R. H. 1967, *Phys. Fluids*, 10, 1417
 Laughlin, G., Steinacker, A., & Adams, F. C. 2004, *ApJ*, 608, 489
 Lesur, G., & Longaretti, P.-Y. 2007, *MNRAS*, 378, 1471
 Lesur, G., & Ogilvie, G. I. 2008, *A&A*, 488, 451
 Lyra, W., Johansen, A., Klahr, H., & Piskunov, N. 2008, *A&A*, 479, 883
 Masset, F. 2000, *A&AS*, 141, 165
 Miller, K. A., & Stone, J. M. 2000, *ApJ*, 534, 398
 Moffatt, H. K. 1978, *Magnetic field generation in electrically conducting fluids* (Cambridge University Press, 1978)
 Nelson, R. P., & Papaloizou, J. C. B. 2004, *MNRAS*, 350, 849
 Oishi, J. S., Mac Low, M.-M., & Menou, K. 2007, *ApJ*, 670, 805
 Parker, E. N. 1955, *ApJ*, 122, 293
 Pringle, J. E. 1981, *ARA&A*, 19, 137
 Rogachevskii, I., & Kleeorin, N. 2003, *Phys. Rev. E*, 68, 036301
 Safronov, V. S. 1969, *Evolutsiia doplanetnogo oblaka*. (English transl.: Evolution of the Protoplanetary Cloud and Formation of Earth and the Planets, NASA Tech. Transl. F-677, Jerusalem: Israel Sci. Transl. 1972)
 Schüssler, M. 1981, *A&A*, 94, L17
 Shakura, N. I., & Sunyaev, R. A. 1973, *A&A*, 24, 337
 Sheehan, D. P., Davis, S. S., Cuzzi, J. N., & Estberg, G. N. 1999, *Icarus*, 142, 238
 Stone, J. M., & Norman, M. L. 1992, *ApJS*, 80, 791
 Sun, Z.-P., Schubert, G., & Glatzmaier, G. A. 1993, *Science*, 260, 661
 Terquem, C., & Papaloizou, J. C. B. 1996, *MNRAS*, 279, 767
 Urpin, V. 2002, *Phys. Rev. E*, 65, 026301
 Vishniac, E. T., & Brandenburg, A. 1997, *ApJ*, 475, 263
 Vishniac, E. T., submitted to *ApJ*
 Weidenschilling, S. J. 1977, *MNRAS*, 180, 57
 Weidenschilling, S. J. 1997, *Icarus*, 127, 290
 Whipple, F. L. 1972, in *From Plasma to Planet*, ed. A. Elvius, 211
 Yoshimura, H. 1981, *ApJ*, 247, 1102
 Youdin, A. N., & Shu, F. H. 2002, *ApJ*, 580, 494
 Youdin, A. N., & Lithwick, Y. 2007, *Icarus*, 192, 588
 Yousef, T. A., Heinemann, T., Schekochihin, A. A., Kleeorin, N., Rogachevskii, I., Iskakov, A. B., Cowley, S. C., & McWilliams, J. C. 2008, *Physical Review Letters*, 100, 184501
 Zheligovsky, V. A., Podvigina, O. M., & Frisch, U. 2001, *Geophysical and Astrophysical Fluid Dynamics*, 95, 227

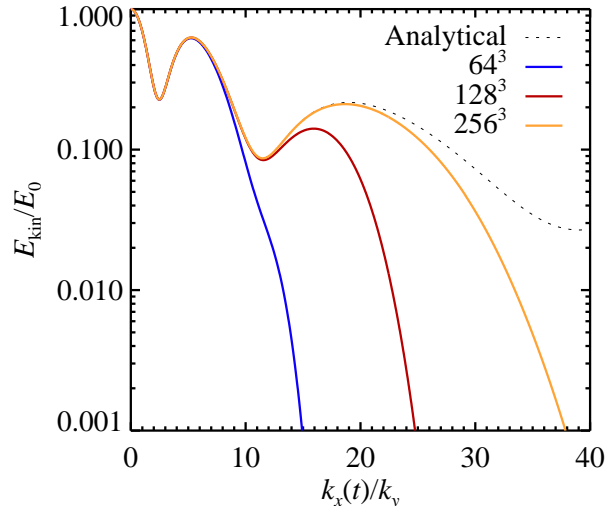


FIG. 12.— Normalized kinetic energy of a time-dependent non-axisymmetric shear wave, for different numerical resolutions and the analytical solution. The numerical solution follows the analytical solution well down to around 6-8 grid points per radial wavelength, after which the explicit viscosity is so strong that the shear wave dies out. There is no evidence of non-linear aliasing as the wave approaches the grid scale, again due to damping by the explicit viscosity terms at the small scales. Compare with Fig. 3 of Balbus & Hawley (2006) which shows the results with the Athena code.

APPENDIX

A. TEST OF SHEARING BOX IMPLEMENTATION

In this Appendix we test the shearing box implementation of the Pencil Code against known analytical solutions to the evolution of shearing waves. In §A.1 we compare the results of the Pencil Code to the analytical solution found by Balbus & Hawley (2006) for hydrodynamical shearing waves. We proceed to test the magnetic field module in §A.2, where we compare a numerical solution of the linearized shearing box MHD equations to the results obtained with the Pencil Code. We find excellent agreement in both cases.

A.1. Time-Dependent Incompressible Shear Wave

Balbus & Hawley (2006) derived a time-dependent, non-axisymmetric and incompressible solution for hydrodynamical shear waves. Solutions are of the form of a single mode $f(x, y, z, t) = \hat{f}(t) \exp[i(k_x(t)x + k_y y + k_z z)]$ for the dynamical variables u_x , u_y and u_z . The Keplerian shear causes the radial wavenumber to be time-dependent and have the form $k_x(t) = k_x(0) + (3/2)\Omega t k_y$.

We have performed numerical simulations of the model set up described in §5 of Balbus & Hawley (2006). We use the simulation parameters $q = 3/2$, $\Omega = 0.001$, $\rho = 1$, $c_s = 4.08\Omega$, $\gamma = 5/3$ and $P = 10^{-5}$. The box size is $L_x = L_y = L_z = 1$. The initial condition is a non-axisymmetric wave in the x -velocity,

$$u_x(x, y, z, t = 0) = A_R \sin[2\pi(y + 4z)], \quad (\text{A1})$$

with the amplitude $A_R = 10^{-5}$.

In Fig. 12 we show the numerical solution for a range of resolutions and compare with the analytical solution. There is excellent agreement between the Pencil Code integration and the analytical solution, down to 6-8 grid points per wavelength where the viscous damping is so strong that the wave dies out. There is no trace of non-linear aliasing as the wave is sheared below the spatial resolution. Balbus & Hawley (2006) show a similar plot for the Athena code in their Fig. 3. Actually the Pencil Code is slightly less dissipative than the Athena code, but this of course depends on our choice of dissipation parameters. For the results in Fig. 12 we set the hyperviscosity and hyperdiffusion similar to their values in the MRI simulations (i.e. similar viscous dissipation time at the grid scale).

A.2. Magnetized Shear Wave in the Linear Regime

To test the evolution of the magnetic vector potential in the shearing box we set up a magnetized shearing wave test problem. Magnetized shear waves are an interesting analytical and numerical topic, but in this appendix we shall consider such waves solely to test the numerical solver of the Pencil Code. We refer to Johnson (2007) for details on the physical behavior of magnetized shear waves.

Linearizing the equation of motion, continuity equation and induction equation as $f = f_0 + f'$ for all components and considering the time evolution of individual Fourier modes of the form

$$f'(x, y, z, t) = \hat{f}(t) \exp[i(k_x(t)x + k_y y + k_z z)], \quad (\text{A2})$$

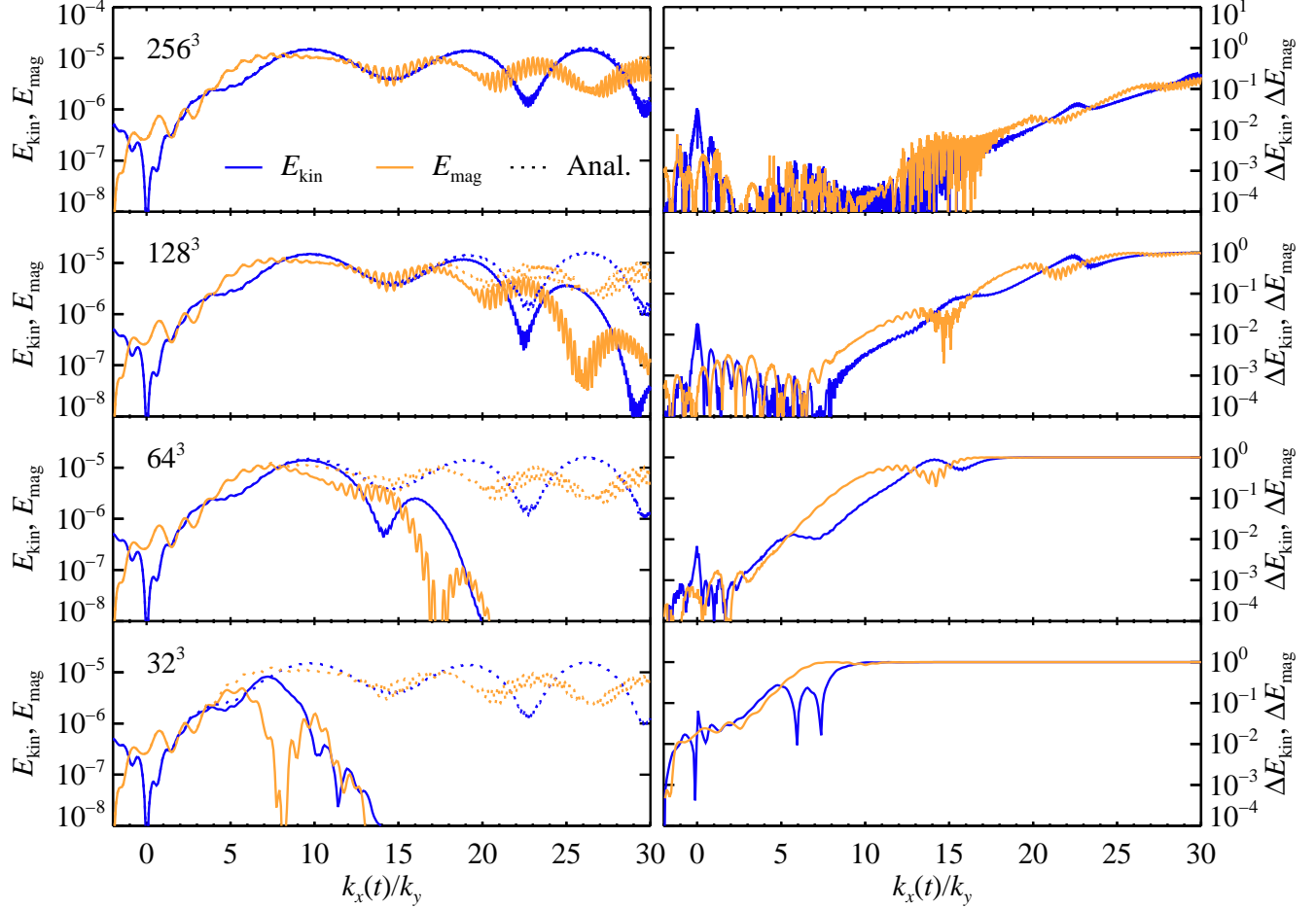


FIG. 13.— Kinetic and magnetic energy of a magnetized, non-axisymmetric shear wave as a function of radial wavenumber (left plots). The relative error between analytical and numerical solution is shown in the right plots (here zero is defined as no error, while an error measure of unity corresponds to infinite error). There is excellent agreement between the numerical solution of the Pencil Code and the analytical solution, down to approximately 6 grid points per wavelength.

with time-dependent radial wavenumber

$$k_x(t) = k_x(0) + \frac{3}{2}\Omega t k_y, \quad (\text{A3})$$

yields

$$\frac{d\hat{\mathbf{u}}}{dt} = 2\Omega\hat{u}_y\mathbf{e}_x - \frac{1}{2}\Omega\hat{u}_x\mathbf{e}_y + \frac{1}{\rho_0} \left[-i\mathbf{k}(\mathbf{B}_0 \cdot \hat{\mathbf{B}}) + i(\mathbf{B}_0 \cdot \mathbf{k})\hat{\mathbf{B}} \right] - \frac{c_s^2}{\rho_0}i\mathbf{k}\hat{\rho}, \quad (\text{A4})$$

$$\frac{d\hat{\rho}}{dt} = -\rho_0 i\mathbf{k} \cdot \hat{\mathbf{u}}, \quad (\text{A5})$$

$$\frac{d\hat{\mathbf{B}}}{dt} = i(\mathbf{B}_0 \cdot \mathbf{k})\hat{\mathbf{u}} - \frac{3}{2}\Omega\hat{B}_x\mathbf{e}_y - i\mathbf{B}_0\mathbf{k} \cdot \hat{\mathbf{u}}. \quad (\text{A6})$$

Setting $\mathbf{B} = (0, 0, B_0)$, $\mathbf{k} = (0, 0, k_z)$, $\hat{\mathbf{u}} = (\hat{u}_x, \hat{u}_y, 0)$ and $\hat{\mathbf{B}} = (\hat{B}_x, \hat{B}_y, 0)$ would yield evolution according to the linear magnetorotational instability (Balbus & Hawley 1991). But since we are interested in the potential effect of shear advection and shear-periodic boundary conditions we instead seed a compressive, non-axisymmetric mode with $\mathbf{k} = [-2, 1, 4]$, $\hat{\mathbf{u}} = [0.001, 0, 0]$, $\rho_0 = 1$, $\mathbf{B}_0 = [0, 1, 0]$, $\hat{\mathbf{B}} = [0, 0, 0]$ in a box of size $(2\pi)^3$. Such a leading wave perturbation of an azimuthal field line is subject to a transient non-axisymmetric magnetorotational instability (Balbus & Hawley 1992; Foglizzo & Tagger 1995; Terquem & Papaloizou 1996). In Fig. 13 we compare the evolution of magnetic and kinetic energy obtained by the Pencil Code to the evolution obtained by integrating the linearized equation system in time. There is excellent agreement between the two down to approximately 6 grid points per wavelength.

B. KEPLERIAN SHEAR ADVECTION AS INTERPOLATION

In this Appendix we describe the numerical implementation of interpolated Keplerian advection in the Pencil Code. The splitting of the advection step into advection by Keplerian shear and advection by the fluctuating velocity goes back to Gammie (2001) for the shearing box approximation and to Masset (2000) for global, cylindrical coordinates. The interpolation scheme was recently generalized to include magnetic fields, in the shearing box approximation, and implemented in a ZEUS-like code by Johnson et al. (2008).

All shearing box dynamical variables f have a Keplerian advection term of the form

$$\frac{\partial f}{\partial t} = -u_y^{(0)} \frac{\partial f}{\partial y} \quad (\text{B1})$$

in their time evolution equation. Here $u_y^{(0)} = -(3/2)\Omega x$ is the linearized Keplerian velocity. The time-step associated with the Keplerian advection is $\delta t = c_{\delta t} \delta x / \max(|u_y^{(0)}|)$, where $c_{\delta t}$ is a factor of less than unity (in the Pencil Code stability requires approximately $c_{\delta t} \leq 0.4$). The Keplerian advection time-step dominates over the time-step from sound waves when $\max(|u_y^{(0)}|) > c_s$, i.e. when $L_x/H > 2/(3/2) \approx 1.33$ for Keplerian rotation.

The time-step of the Keplerian advection is irrelevant if that term is not treated by finite-differencing, but rather as a shift of all variables in physical space by the amount $u_y^{(0)} \delta t$. Without deriving it formally we can estimate that the stability criterion with this method is that neighboring points in the x -direction must not move more than a fraction ξ of a grid point apart,

$$(3/2)\Omega \delta x \delta t < \xi \delta y. \quad (\text{B2})$$

This is a much less tight time-step constraint than for the finite difference approach, since there is no longer any reference to the radial coordinate x in the time-step calculation. The interpolation scheme also eliminates the numerical diffusivity associated with the Keplerian advection (see Appendix C).

We implement the interpolated Keplerian advection as follows:

1. All variables $q(x, y, z)$ are Fourier transformed in the y -direction to yield $\hat{q}(x, k_y, z)$.
2. Each Fourier amplitude is multiplied by the complex factor $\exp[ik_y u_y^{(0)}(x) \delta t]$ to shift by the amount $u_y^{(0)}(x) \delta t$ in real space.
3. Inverse Fourier transform to real space.

Because of the third order Runge-Kutta time-integration scheme of the Pencil Code, the shift must be done for the inherited right-hand-sides \hat{q} at the beginning of the second and third sub-time-steps as well. The time-step entering in point 2 above, now dominated by sound waves, is calculated at the first sub-time-step of the Runge Kutta scheme and consequently used for all three substeps, including the Keplerian advection.

Note that in Masset (2000) the state is always shifted by an integer number of grid points, treating the remaining Keplerian advection speed together with the perturbed speed. In this paper, on the other hand, the entire Keplerian advection is done by interpolation in Fourier space. We denote this scheme Shear Advection by Fourier Interpolation (SAFI).

C. REMOVING POSITION-DEPENDENT NUMERICAL DIFFUSIVITY

In this Appendix we quantify the numerical diffusivity of the Pencil Code advection scheme and, very importantly for simulations of turbulence in large shearing boxes, its dependence on the background advection speed. We show how to eliminate the spatial dependence of the numerical diffusivity by various improvements to the shearing box algorithm of the Pencil Code.

C.1. Measuring the Numerical Diffusivity of the Pencil Code

Although numerical diffusion is not necessarily representable as a well-behaved differential operator, we shall fit the time evolution of a passively advected physical variable f according to the expression

$$|\hat{f}|(t) = |\hat{f}|(0) \exp(-D_n k^{2n} t). \quad (\text{C1})$$

The hat denotes here that f is set as a pure Fourier mode at scale k , and D_n is a diffusivity coefficient of order n . Regular diffusion would e.g. have $n = 1$, while hyperdiffusion has higher values of n .

We measure the diffusivity of the Pencil Code's advection scheme by advecting a wave of arbitrary initial amplitude for the time $\Delta t = 100$ with the constant advection speed u_0 . We then fit the amplitude reduction parameter,

$$Q = -\ln \left(\frac{|\hat{f}|(\Delta t)}{|\hat{f}|(0)} \right), \quad (\text{C2})$$

according to the power law

$$Q \propto k^{2n} u_0^m (\delta t)^l. \quad (\text{C3})$$

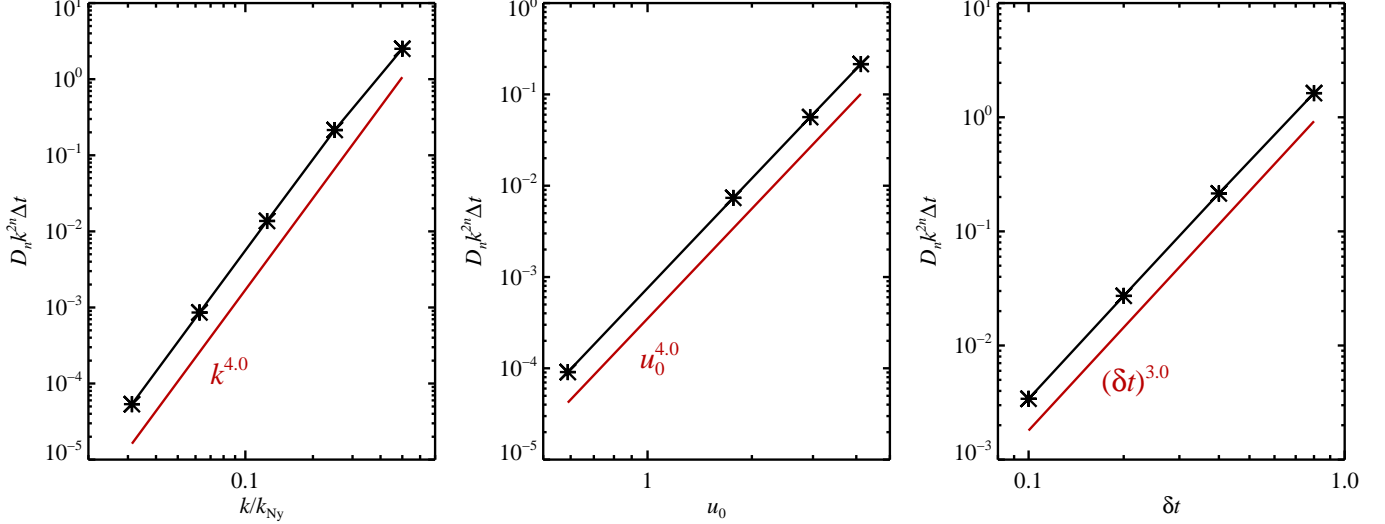


FIG. 14.— The dependence of the amplitude reduction parameter $Q = D_n k^{2n} \Delta t$ on wavenumber k (first plot), advection speed u_0 (middle plot) and time-step δt (last plot). All dependencies are fitted excellently by a power-law, indicating an numerical diffusivity that behaves like second order hyperdiffusivity.

Here δt is the time-step of the temporal integration. If the wavenumber-dependence can indeed be fitted with a single n , then the diffusion coefficient is fitted according to $D_n \propto u_0^m (\delta t)^l$. We show in Fig. 14 the dependence of Q on k , u_0 and δt . There is an extremely good power-law fit for each parameter, with $n = 2$, $m = 4$ and $l = 3$. Thus the numerical diffusivity behaves like a second order hyperdiffusion,

$$\dot{f} = -D_2 \frac{\partial^4 f}{\partial y^4}, \quad (\text{C4})$$

with diffusion coefficient

$$D_2 \approx 0.041 u_0^4 (\delta t)^3. \quad (\text{C5})$$

One may in fact show from stability analysis that $D_2 = (1/24) u_0^4 (\delta t)^3$ (W. Dobler, private communication). The strong dependence on the time-step δt is not surprising for the 3rd order Runge-Kutta scheme of the Pencil Code. One consequence is that if δt is determined from the global maximum speed, and u_0 varies across the simulation domain, then the diffusion coefficient goes as the background speed to the fourth power, which can lead to huge differences in the numerical diffusivity across the box.

C.2. Improved Shearing Box Algorithms

We proceed to test the effect of the varying numerical diffusivity in a linear shear flow. We have set up a simple advection test where a wave of azimuthal wavelength 8 grid points is advected by a linear shear flow with velocity difference $(3/2)\pi \approx 4.71$ from box edge to box center (the radial extent of the box is $L_x = 2\pi$). We follow the amplitude of the wave as a function of the distance from the center of the box. This is plotted in Fig. 15. The first panel shows that for the usual advection scheme the error grows much quicker near the box edges, while the box center is left almost untouched by numerical diffusion⁸.

There are several ways to reduce, or even remove, this space-dependent numerical diffusivity. Here we discuss three ways:

1. Picking the center of revolution randomly at each time-step, thus making sure that even the central points are advected by the shear.
2. Displacing the entire data cube by one grid point in the radial direction in the beginning of each time-step.
3. Treating the shear advection term separately by high order interpolation.

C.2.1. Random Revolution Center (RRC)

The linear shear flow can be generalized as

$$u_y^{(0)} = -\frac{3}{2} \Omega (x - x_0), \quad (\text{C6})$$

where x_0 is the radial coordinate of the revolution center, normally set to zero. We can nevertheless choose an arbitrary $x_0 \in [-L_x/2, L_x/2]$ at each time-step and still solve exactly the same equation system. This way we can reduce the

⁸ The central grid points $i = 3, 4$ lie at both sides of $x = 0$, thus even these grid points experience some shear advection.

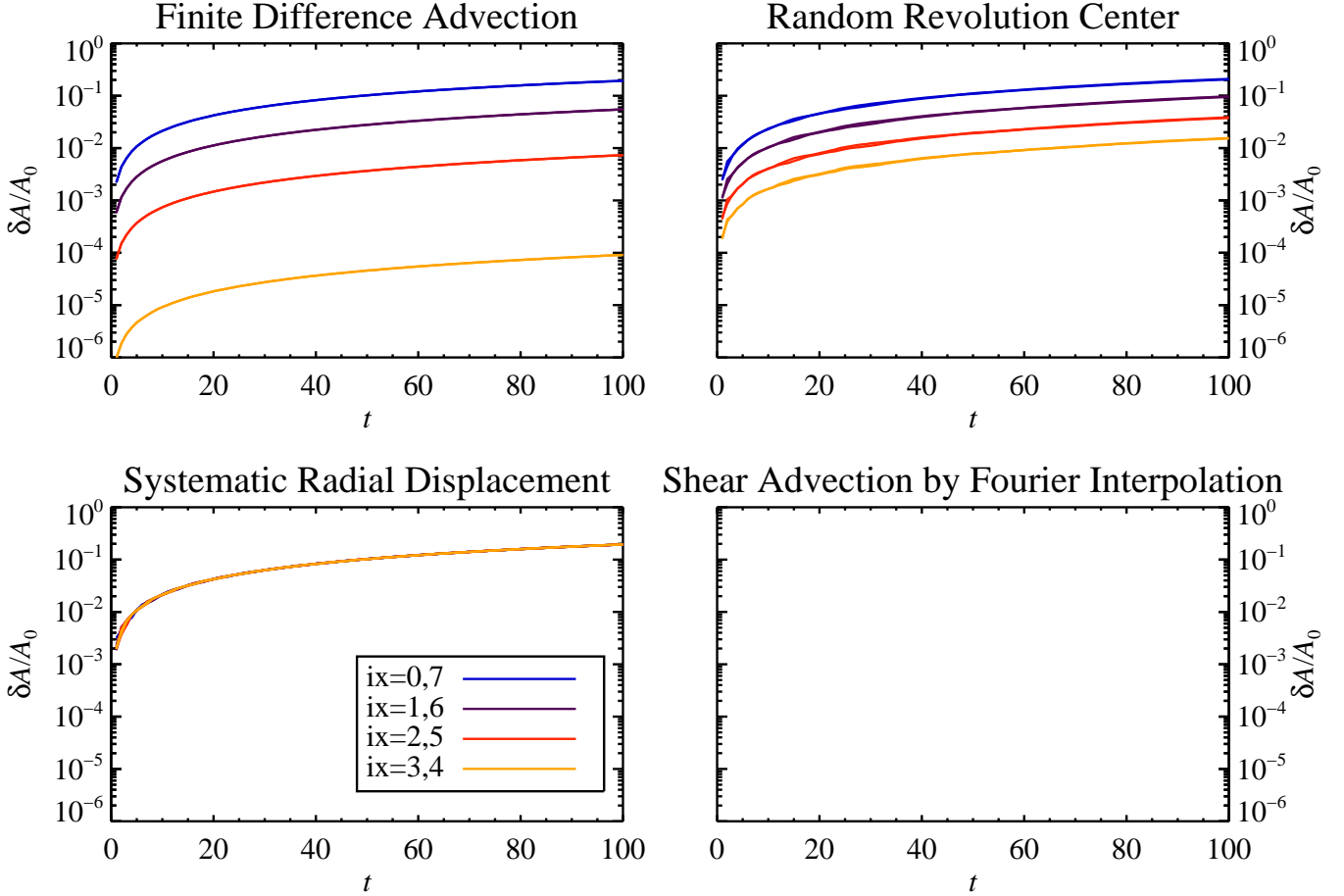


FIG. 15.— The amplitude of a passively advected shear wave as a function of time t at four radial positions in the box (different colors). The amplitude falls due to the numerical diffusivity associated with the Keplerian advection term. The simple finite difference scheme gives much higher error near the edges of the box (first plot), as the numerical viscosity scales with the local advection speed to the fourth power. Centering the shear around a random point in the box increases the error in the center (second plot), but the error maintains a significant dependence on the radial coordinate. By displacing the entire data cube by one grid point in the radial direction in the beginning of each time-step or by interpolating the shear advection term in Fourier space one can remove the radial dependence of the amplitude error (third and fourth plots).

special state that $x = 0$ normally has because that point is not advected. The second plot of Fig. 15 shows the radially dependent amplitude error using the Random Revolution Center scheme. While the error near the center is greatly increased compared to the usual advection scheme, there is still a significant difference in the amplitude between the center and the edges of the box.

The time-step constraint of the RRC method is slightly tighter than for the usual advection scheme, since the maximum advection speed is around a factor two times higher. The higher average advection speed leads to some increase in the overall numerical diffusivity, although the lower time-step partially counteracts this increase.

C.2.2. Systematic Radial Displacement (SRD)

A better way to reduce the radially dependent numerical diffusivity is to distribute the error over the entire box. We do this by shifting the data cube by one grid point in the radial direction at the beginning of each (main) time-step. In the time interval $\Delta t = N_x \delta t$ a physical structure will have experienced numerical diffusivity at all radial locations in the box, and since this is much shorter than the relevant physical time-scale $2\pi\Omega^{-1}$, the total numerical diffusivity should be approximately the same for all flow features. In the third plot of Fig. 15 we show how all grid points have the same amplitude error, even after a long integration time. The time-step may furthermore be lowered artificially in order to reduce the time spent at any given radial location. This method is preferred over the Random Revolution Center scheme, but at the cost of a slightly higher numerical diffusivity as the shearing radial boundary conditions must be set twice each time-step. Also postprocessing and on-the-fly diagnostic output is complicated by the rapid radial displacement of the grid.

C.2.3. Shear Advection by Fourier Interpolation (SAFI)

A third possibility is to reduce amplitude error in the advection scheme through time integration of the Keplerian advection term by interpolation. The Shear Advection by Fourier Interpolation scheme is described in detail in

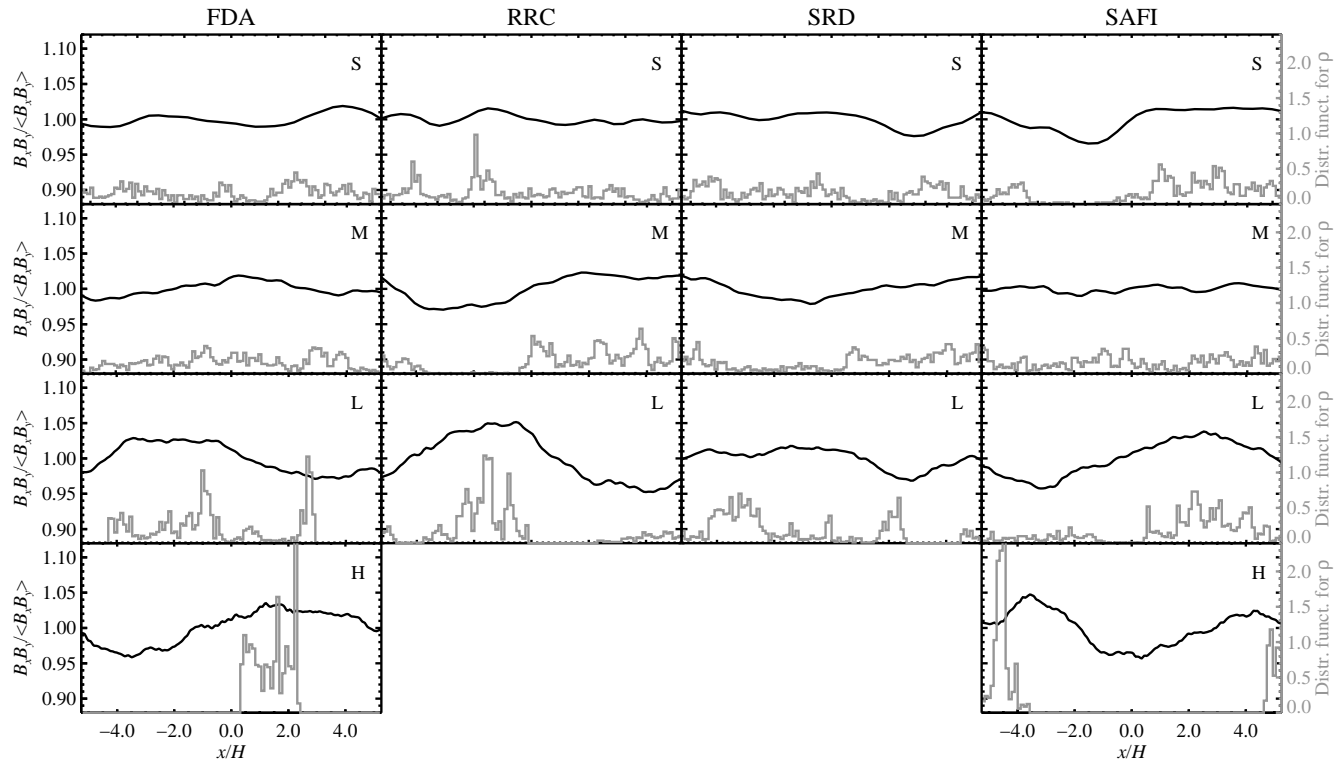


FIG. 16.— The Maxwell stress, divided by the mean Maxwell stress, as a function of the radial distance from the center of the box (black curve). Overplotted is the distribution function for the location of the minimum of the largest radial density mode (gray histograms). Rows represent various box sizes, while columns show the results for Finite Difference Advection (FDA), Random Revolution Center (RRC), Systematic Radial Displacement (SRD), and Shear Advection by Fourier Interpolation (SAFI). The typical fluctuation in the Maxwell stress is in all cases around 10% (see Table 3). In the smallest boxes these fluctuations have almost canceled out each other, since the correlation time of the stress is so short. The two largest boxes, on the other hand, have an excess of a few percent. Here the 100 orbits integration has not covered enough coherence time-scales to give a good average. There is a slight tendency for the turbulence to be weak near the edges of the box, and for the density minimum to appear near the center of the box, when using the standard finite difference advection scheme (FDA, first column).

Appendix B where we focused on making to allowed time-step longer by integrating the Keplerian advection term through high order interpolation. This scheme however also reduces the amplitude error of the advection to zero, yielding a numerical diffusivity that does not depend on the radial coordinate. The last panel of Fig. 15 shows that the amplitude error is indeed zero with this scheme.

In fact the SAFI method advects all scales with zero amplitude error and zero dispersion error. The only exception is the Nyquist scale, which is damped as the wave approaches a cosine function of y . This process of damping power at the Nyquist scale can have a stochastic element to it, as it may take arbitrarily long for the sine wave to be mapped as a cosine wave on the grid.

So in effect there will be an x -dependent amplitude error at the Nyquist scale. This is however unlikely to affect the overall diffusivity of the Keplerian advection, since the Nyquist scale is already heavily damped by the explicit (hyper, shock, or regular) diffusivity terms. A combination of the SRD and SAFI schemes would in theory remove the x -dependent damping of the Nyquist scale, but we have not explored this any further since the SRD scheme complicates postprocessing significantly.

C.3. Comparison of Results Obtained with Various Shearing Box Schemes

To test the relevance of space-dependent numerical dissipation for our results we have run four variations of each of the standard box sizes S, M, L (FDA, RRC, SRD, SAFI), and two variations of the largest box H (FDA, SAFI). The Maxwell stress, normalized by the mean Maxwell stress, is shown in Fig. 16 as a function of radial distance from the center of the box. We have overplotted the distribution function for the location of the minimum of the largest radial density mode (see histograms and the right axis). For the standard finite difference advection scheme there is a tendency for the turbulence to be weaker near the edges of the box and for the density minimum to occur near the center of the box (see first column). However, the preference for turbulence to be strong near the box center is not consistently present with any of the improved shearing box algorithms. Thus we conclude that space-dependent numerical diffusivity can potentially lead to spurious flow features for large shearing boxes with the Pencil Code, but that this problem is alleviated by either displacing the grid systematically in the radial direction at each time-step or by integrating the Keplerian advection term by Fourier interpolation.

The measured statistical properties of zonal flows, pressure bumps and large scale power for various shearing box

algorithms are written in Table 4. For each box size there is a tendency for the large scale power in zonal flows and pressure bumps to decrease when going from the standard finite difference advection scheme to the Fourier interpolation method. The amplitude of the Maxwell stress, on the other hand, is relatively independent of the chosen algorithm. Based on these measurements we found it safer to use the Fourier interpolation scheme for box sizes L and H.